

Hourly Assimilation of Different Sources of Observations Including Satellite Radiances in a Mesoscale Convective System Case During RELAMPAGO campaign

Paola Belén Corrales^{a,b,c}, Victoria Galligani^{a,b,c}, Juan Ruiz^{a,b,c}, Luiz Sapucci^f, María Eugenia Dillon^{d,e}, Yanina García Skabar^{d,e,c}, Maximiliano Sacco^d, Craig S. Schwartz^g, Stephen W. Nesbitt^h

^aUniversidad de Buenos Aires, Facultad de Ciencias Exactas y Naturales, Departamento de Ciencias de la Atmósfera y los Océanos. Buenos Aires, Argentina.

^bCONICET – Universidad de Buenos Aires. Centro de Investigaciones del Mar y la Atmósfera (CIMA). Buenos Aires, Argentina.

^cCNRS – IRD – CONICET – UBA. Instituto Franco-Argentino para el Estudio del Clima y sus Impactos (IRL 3351 IFAECI). Buenos Aires, Argentina.

^dServicio Meteorológico Nacional de Argentina.

^eCONICET (Consejo Nacional de Investigaciones Científicas y Técnicas).

^fNational Institute for Space Research, Brazil, Center for Weather Forecasting and Climate Studies.

^gNational Center for Atmospheric Research, Boulder, Colorado.

^hDepartment of Atmospheric Sciences, University of Illinois Urbana-Champaign, Urbana, Illinois.

Abstract

In this paper, we evaluate the impact of assimilating high-resolution surface networks and satellite observations using the WRF-GSI-LETKF over central and north eastern Argentina where the surface and upper air observing networks are relatively coarse. We conducted a case study corresponding to a huge mesoscale convective system (MCS) that developed during November 22, 2018. The accumulated precipitation associated with this MCS was quite high, exceeding 200 mm over northern Argentina and Paraguay. The MCS developed during the Intense Observing Period (IOP) of the Remote sensing of Electrification, Lightning, And Mesoscale/microscale Processes with Adaptive Ground Observations (RELAMPAGO) field campaign. We used the GSI-4DLETKF data assimilation package to produce analyses by assimilating observations every hour with 10-km horizontal grid spacing and a 60-member multiphysics ensemble. We conducted four assimilation experiments using different sets of observations: CONV, consisting of conventional observations from NCEP's prepBUFR files; AWS, combining CONV and dense automatic surface weather station networks, SATWND, combining AWS with satellite-derived winds, and RAD, including SATWND; and satellite radiances from different microwave and infrared sensors. We found that the assimilation of observations with high temporal and spatial frequency generate an important impact on the PBL, primarily on the precipitable water content, that leads to the development of deep convection and heavy precipitation closer to the observed in this case study. The assimilation of radiance observations produces a better development of the convection mainly during the mature state of the MCS leading to an increase in the accumulated precipitation. We also ran ensemble forecasts initialized from each experiment and evaluated their skill to predict precipitation. We found that the hourly assimilation of the observations in AWS, SATWND, and RAD helped to improve the precipitation forecast.

Key words: Regional Data Assimilation, Surface Observations, Satellite Observations

1. Introduction

Severe weather events cause significant human and economic losses around the world. A large number of these phenomena are associated with the occurrence of deep moist convection, including tornadoes, intense wind gusts, extreme precipitation in short time periods, large hail, and lightning. Southern South America has one of the highest frequencies in the world of favorable conditions for high-impact meteorological events [Brooks et al.] and large hail events [Cecil and Blankenship], particularly during austral spring and summer. This is also confirmed by observational evidence and high impact weather reports [Matsudo et al.,

Rasmussen et al.]. Recently, the RELAMPAGO-CACTI field campaign [Nesbitt et al.] has been conducted to investigate the mechanisms for convective initiation and the occurrence of high-impact weather events associated with deep convection in central Argentina.

Forecasting mesoscale meteorological phenomena and particularly deep moist convection is a scientific and technological challenge due to its limited predictability and the difficulties in diagnosing the state of the atmosphere at small spatial and short temporal scales (for example from 1 to 10 kilometers and on the order of minutes). Mesoscale data assimilation (DA) is an approach that can provide appropriate initial conditions for high-resolution numerical forecasts [Sun et al.] and thus has received increasing attention in the last decades.

For DA methods to be successful, observing networks

*Corresponding Author

Email address: paola.corrales@cima.fcen.uba.ar (Paola Belén Corrales)

with sufficient temporal and spatial resolution capable of capturing mesoscale variability should be used (?). In that regard, several authors investigated the impact of assimilating surface weather data (e.g. Wheatley and Stensrud, Ha and Snyder, Chang et al., Bae and Min, Banos et al., Maejima et al., and Chen et al. [b]) using different simulation methodologies. Most of these studies reported the beneficial impacts of assimilating temperature and dew point observations upon the planetary boundary layer structure and the location and timing of precipitating systems. Sobash and Stensrud showed using a mesoscale DA system, that the positive impact upon convection initiation and the short range precipitation forecast is achieved if data is assimilated frequently (in the order of minutes, rather than in the order of hours). More recently, Gasperoni et al. evaluated the impact of assimilating observations produced by private weather station networks which are not incorporated in the operational analysis. They found a positive effect of these observations upon the initiation of deep moist convection. This result is particularly important for data sparse regions such as Southern South America, where operational networks are not dense enough to capture mesoscale details.

The impact of other types of high spatial and temporal resolution observations, such as atmospheric motion vectors (AMVs), has also been investigated in the context of limited-area mesoscale DA. Many studies have focused on the impact of these observations on the prediction of tropical storms (e.g., Wu et al., Cherubini et al., and Sawada et al., and many others). Most of these studies reported an overall positive impact of the assimilation of AMVs for this type of storm. However, some works indicated mixed impacts (e.g. Sawada et al. reported an improvement in the forecast of the track of the storm but a degradation in the forecast intensity). As stated in Zhao et al. [a] and Zhao et al. [b], the impact of assimilating these data on high impact weather events associated with mid-latitude deep convection over land has received relatively less attention. Zhao et al. [a,b] assimilated GOES-16 AMVs into a storm-scale three-dimensional variational DA system during three high impact weather events. They reported positive impacts of AMVs on the characterization of the storm environment and improved short range precipitation forecasts. Otsuka et al. and Mallick and Jones found a slight improvement in the short-range precipitation forecast due to the storm-scale assimilation of high frequency AMVs.

While the assimilation of radiance observations into global models is well established [Eyre et al.], the direct assimilation of radiance data into regional models, however, still remains a challenge due to the sparse data coverage (in the case of polar-orbiting satellite observations), bias correction, and the relatively low model tops used for this application. Bao et al. studied the impact of assimilating microwave and infrared radiance data on temperature and humidity forecasts over the western USA and found a reduction in the temperature bias at low and mid-levels as

result of the microwave observations but an opposite effect for infrared data. More recently, Zhu et al. [a] studied the impact of assimilating satellite radiance data within a frequently updated regional system and showed an improvement for all variables, in particular for relative humidity at upper levels. Wang and Randriamampianina studied the impact of assimilating radiances in the high-resolution Copernicus European Regional Reanalysis. They reported that satellite radiance observations had a neutral impact on the analyses of geopotential height in the lower troposphere, while a slightly negative impact on the upper troposphere and the stratosphere. They also observed similar results for 3-h forecasts initialized from the analysis but a positive impact on 12 and 24 -h forecasts. Given these mixed results, there is still room to analyze the utility of assimilating radiance observations in a limited-area DA system over land. Moreover, to the best of our knowledge, there are no studies related to the direct assimilation of radiance observations over South America.

In particular, in South America, the relatively scarcity of conventional observations such as radiosondes increases the potential impact of the observation sources previously discussed. Previous work has shown promising results of mesoscale DA in South America using some of the above mentioned data sources [e.g. Dillon et al., a,b, Goncalves de Goncalves et al.]. In particular Dillon et al. [b] assimilated high resolution surface weather station networks, GOES-16 AMVs, and satellite temperature and moisture retrievals with promising results. However, no work has been conducted yet over this region to investigate the potential contribution of the datasets discussed above. The main objective of this work is to contribute to the quantification and comparison of the impact of high resolution surface weather stations, AMVs, and clear-sky satellite radiances, into a mesoscale, frequently-updated ensemble-based DA system. In particular, we will focus on the impact in the context of mid-latitude mesoscale convective system events. Another particular goal of this paper is to investigate the impact of these data sources in a region where the conventional observation network is rather sparse and where the potential contributions of these observing systems is larger.

To reach this goal, we conduct several DA experiments for a case study of a large Mesoscale Convective System (MCS) that developed over Southern South America during Nov 22-23, 2018 during the intense observation period (IOP) of the RELAMPAGO field campaign.

The paper is organized as follows. The DA system, the experimental design, and the observations used are presented in section 2. Results are discussed in section 3 and finally, conclusions are summarized in section 4.

2. Data and Methods

2.1. Case overview

Previously to the development of this case study, the center and north of Argentina was immersed in a warm and

humid air mass with high values of convective available potential energy (CAPE) (Figure 1a). On Nov 22, 2018 a cold front crossed the center of Argentina triggering isolated convective cells (Figure 1b) that rapidly grew upscale into an exceptionally large MCS. During that day several surface stations reported lightning, gustfronts and heavy rain. To the north of the region, a warm front contributed to the development of isolated multicells that ultimately grew and merged with the MCS (Figure 1c). The MCS traveled approximately 2500 km from south to north, dissipating over Paraguay and Southern Brazil after 42 hours.

2.2. Data assimilation system configuration

The forecast model uses the non-hydrostatic Advanced Research version of Weather Research and Forecasting (WRF-ARW V3.9.1, Skamarock et al.). The horizontal grid spacing is 10 km (150 x 200 grid points) in the horizontal and 37 levels in the vertical with the top of the model at 50 hPa. The initial and boundary conditions are provided by the Global Forecast System (GFS) analysis (0.25° horizontal grid spacing and 6-hour temporal resolution, National Centers for Environmental Prediction, National Weather Service, NOAA, U.S. Department of Commerce). The domain covers the area indicated in Figure 2 to capture the development of the MCS during the simulated period.

The analyses are generated using the LETKF implementation (V1.3, Hunt et al.) of the Gridpoint Statistical Interpolation analysis system (GSI V3.8; Shao et al.). A rapid update cycle approach is implemented with hourly analysis and a centered assimilation window, meaning that all the observations within ± 30 minutes of the analysis time are assimilated. Observations are assimilated in a 4D approach by comparing them with the corresponding first-guess state at 10-minute intervals. For radiance observations, the Community Radiative Transfer Model version 2.3 (CRTM; Han et al.) is used as an observation operator to calculate model-simulated brightness temperatures.

We use a 60-member ensemble where the ensemble mean at the beginning of the DA cycle is initialized using the GFS deterministic analysis with random perturbations to generate the initial ensemble perturbations. The perturbations are generated as scaled differences between two random atmospheric states obtained from the Climate Forecast System Reanalysis (CFSR) data with 0.5° horizontal grid spacing with a smooth time evolution as in Necker et al. and Maldonado et al.. In this way, we preserved the nearly hydrostatic and geostrophic equilibrium of larger scales. This method helps to prevent an underestimation of the ensemble spread [Ouaraini et al.]. All experiments presented here uses the same boundary conditions from GFS, generated using the same method as for the initial conditions to maintain proper levels of ensemble spread within the domain.

We used multi-physics scheme to better represent the uncertainty in the model formulation within the DA system. We generated 9 different model configurations consisting of the combination of 3 moist convection schemes

Table 1: Generation of the 60-member RRR multi-physics ensemble as a combination of Cumulus and PBL parameterizations, and GEFS members for boundary conditions.

Cumulus	PBL		
	MYJ	MYNN2	YSU
BMJ	5, 14, 23, 32, 41, 50, 59	8, 17, 26, 35, 44, 53	2, 11, 20, 29, 38, 47, 56
GF	6, 15, 24, 33, 42, 51, 60	9, 18, 27, 36, 45, 54	3, 12, 21, 30, 39, 48, 57
KF	4, 13, 22, 31, 40, 49, 58	7, 16, 25, 34, 43, 52	1, 10, 19, 28, 37, 46, 55

(Kain–Fritsch [Kain], Grell–Freitas [Grell and Freitas], and Betts–Miller–Janjic [Janjić]) and 3 planetary boundary layer schemes (Yonsei University Scheme [Hong et al., b], Mellor–Yamada–Janjic Scheme [Janjić], and Mellor–Yamada Nakanishi Niino [Nakanishi and Niino]). The distribution of these schemes among the 60 ensemble members is outlined in Table 1. The multi-physics approach is also introduced in order to represent the uncertainty associated with the more relevant physical processes that are not resolved by the model. All ensemble members use the same land-surface model (Noah-MP, Chen and Dudhia), microphysics (WRF single-moment 6-class scheme [Hong et al., a]), and radiation processes (RRTMG shortwave and longwave scheme [Iacono et al.]) parameterizations.

To reduce the effect of spurious correlations in the estimation of error covariances, we use a horizontal localization radius of 180 km and a vertical localization radius of 0.4 (in log pressure coordinates) as in Dillon et al. [b] for all types of observations. A relaxation-to-prior spread inflation [Whitaker and Hamill] is applied with an inflation parameter $\alpha = 0.9$ to mitigate the impact of sampling errors and to consider model errors not accounted for by the multi-model ensemble approach.

2.3. Observations

2.3.1. Conventional

The conventional observations used are part of the Global Data Assimilation System (GDAS) data stream. We assimilated conventional observations included in the Binary Universal Form for Representation of Meteorological Data (PREPBUFR) files generated at the National Centers for Environmental Prediction (NCEP). These consist of surface observations from 117 Conventional Surface Weather Stations (CSWS), ships, and upper-air observations from 13 radiosondes sites and aircraft. The orange triangles in Figure 2a indicate the location of the surface stations included in this experiment. The frequency of these observations varied between 1 hour for surface stations and 12/24 hours for radiosondes. Wind surface observations over oceans (ASCATW) come from scatterometers and are also included in the PREPBUFR files.

Table 2 lists all the observation types (i.e., surface pressure, temperature, specific humidity, and wind) available for each source, together with their associated errors. The observation errors were specified following the GSI default

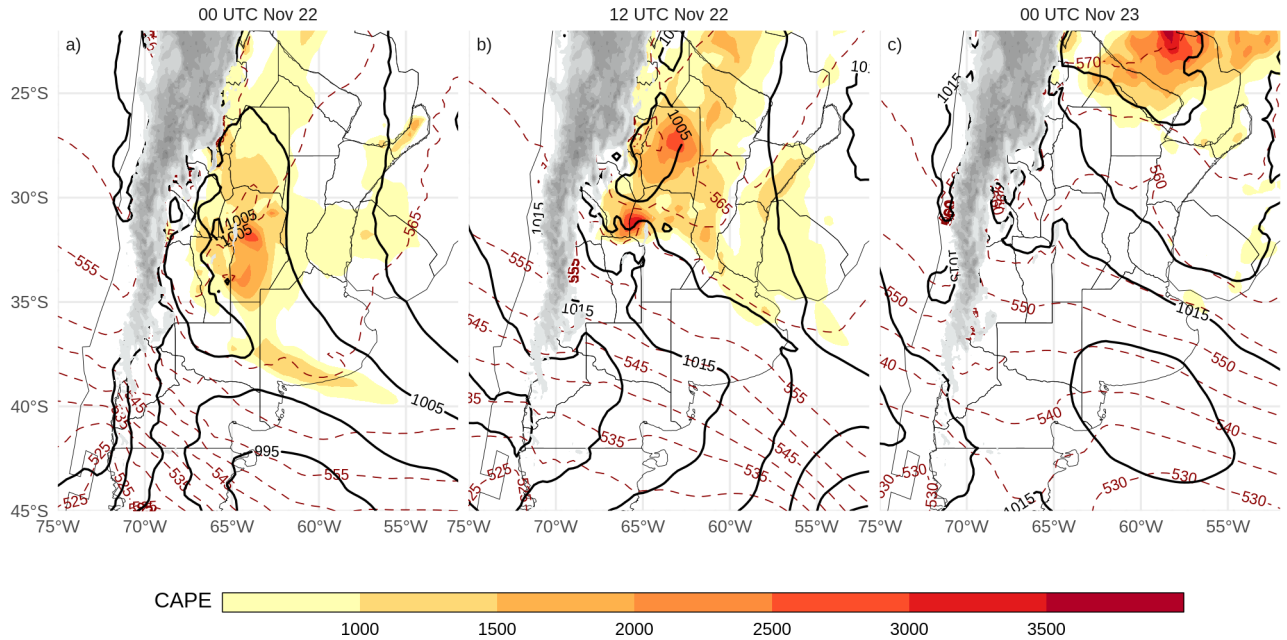


Figure 1: ERA5 Reanalysis of pressure (hPa) at sea level (black contours), 1000-500 hPa thickness (red dashed contours) and convective available potential energy (shaded) for 00 and 12 UTC Nov 22 and 00 UTC Nov 23.

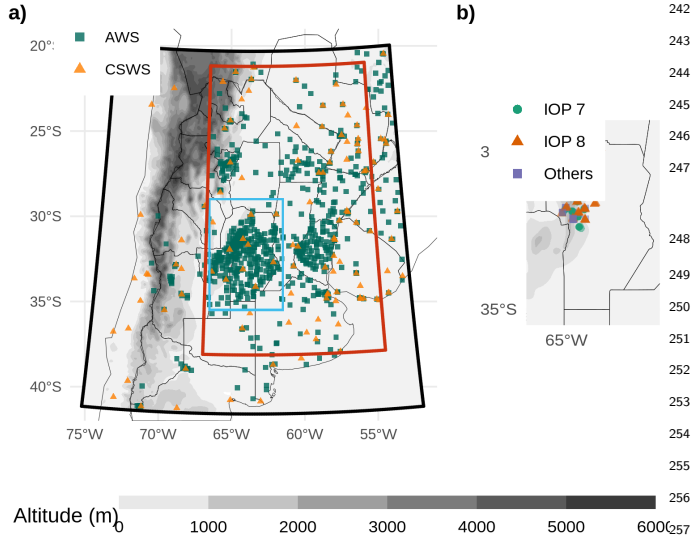


Figure 2: a) The domain used for the simulations (black box), the inner domain used for the experiment comparison (red box), the region shown in b) (light blue box), and the locations of Automatic Weather Stations (AWS, green squares) and Conventional Surface Weather Stations (CSWS, orange triangles). b) Locations of radiosonde launches during RELAMPAGO. Green dots correspond to radiosondes launched during IOP 7, orange triangles are radiosondes launched during IOP 8, and purple squares are radiosondes launched outside the IOP missions. The topography in meters is also shown (shaded).

240 configuration. In some cases, the error varies with height
241 and depends on the specific platform (aircraft and satellite-
242 derived wind). In terms of quality control, a gross check
243 was performed by the observation operator by comparing
244 the innovation (the difference between the observation and
245 the model-simulated observation based on the first-guess)
246 with a predefined threshold that depends on the observation
247 error (also included in Table 2).

2.3.2. AWS networks

We also assimilate data from 866 Automatic Weather Stations (AWS) that are part of 17 public and private surface networks over Southern South America. The dataset used in this study has been obtained from the RELAMPAGO Data Set repository [Garcia et al.]. These stations are indicated as green squares in Figure 2a. They have higher spatial coverage than the CSWS and a sampling frequency of 10 minutes in most cases. All stations measure temperature, but only 395 stations provide humidity, 422 provide pressure, and 605 provide wind information. Observation errors used to assimilate these observations are the same as for the CSWS (see Table 2).

2.3.3. Satellite derived winds

Satellite-derived wind observations are also included in the PREPBUFR files available every 6 h, and consist of estimations from GOES-16 (using the visible, infrared, and water vapor channels) and METEOSAT 8 and 11 (using the visible and water vapor channels). Due to the domain covered by each of these satellites, GOES-16 is the primary source of satellite-derived winds (99 % of the observations).

Table 2: Characteristics of the assimilated observations: The code for each observation type and its source, the available variables, the observation error, and the gross check thresholds used.

Code	Platform	Variable	Error	Gross check
CSWS AWS	Surface weather stations	Pressure	1-1.6 hPa*	3.6 hPa
		Temperature	1.5 K	7 K
		Specific humidity	20 %	8 gKg ⁻¹
		Wind	2.2 ms ⁻¹	6 ms ⁻¹
ADPUPA	Radiosondes	Pressure	1.1-1.2 hPa**	4 hPa
		Temperature	0.8-1.5 K*	8 K
		Specific humidity	20 %	8 gKg ⁻¹
		Wind	1.4-3 ms ⁻¹ *	8 ms ⁻¹
AIRCFT	Aircrafts	Temperature	1.47-2.5 K ⁺	7 K
		Wind	2.4-3.6 ms ⁻¹ +	6.5-7.5 ms ⁻¹ +
ASCATW	Advanced Scatterometers	Wind	1.5 ms ⁻¹	5 ms ⁻¹
SFCSHP	Ships and Buoys	Pressure	1.3 hPa	4 hPa
		Temperature	2.5 K	7 K
		Specific humidity	20 %	8 gKg ⁻¹
		Wind	2.5 ms ⁻¹	5 ms ⁻¹
SATWND	Satellite-derived winds	Wind	3.8-8 ms ⁻¹ **+	1.3-2.5 ms ⁻¹ +

* Observation error varied with height.

** Observations above 600 hPa are rejected.

+ Observation error depends on the report type.

step in the assimilation of radiances, was performed within the GSI system for each sensor specifically. First, a spatial data thinning is applied using a 60 km grid following Singh et al., Jones et al., and Lin et al., where the observations to be assimilated are chosen based on their distance to the model grid points, the observation quality (based on available data quality information), and the number of available channels (from the same pixel and sensor) that passed the quality control. Also, observations over the sea are preferred to those over land or snow [Hu et al.].

The thinned observations were then bias corrected. The bias correction (BC) has an air-mass dependent and an angle-dependent component [Zhu et al., b] and it is calculated as a multi-linear function of N predictors $p_i(x)$, with associated coefficients β_i . Then, the bias corrected brightness temperature (BT_{bc}) can be obtained as:

$$BT_{bc} = BT + \sum_{i=0}^N \beta_i p_i(x) \quad (1)$$

GSI has a constant offset bias correction term ($p_0 = 1$) and the remaining predictors are the cloud liquid water content (CLW), the temperature lapse rate at the pressure of maximum weight, the square of the temperature lapse rate at the pressure of maximum weight, and the emissivity sensitivity. Scan angle-dependent bias is modeled as a 4th-order polynomial [Zhu et al., b].

In the GSI system, the β_i coefficients are trained using a variational estimation method which solves the β_i that provides the best fit between the simulation and the observations. The coefficients were initialized at 18 UTC Nov 18, 2018 with the GFS system coefficients. The assimilation system was configured to use a constant background error variance of 0.01 to avoid large adjustments in the estimated coefficients at each time.

In our experiments, only clear-sky observations are used. For microwave radiances, observations potentially contaminated by clouds are detected using the scattering and Liquid Water Path (LWP) indexes [Weston et al., Zhu et al., c]. For the infrared channels, cloud contaminated observations are detected using the transmittance profile calculated within the CRTM algorithms. Moreover, GSI checks the difference between the observations and simulated brightness temperature with height to detect cloudy pixels. Additionally, the GSI quality control for infrared sensors looks for observations over water with a large zenith angle (over 60°) to reject channels near the visible range that can be contaminated with reflection. It also performs an emissivity check for observations over land for both infrared and microwave radiances.

2.3.5. Validation dataset

To evaluate the performance of the ensemble-based DA system presented in this article, we use the following observational datasets:

- ERA5 hourly data on pressure levels from 1959 to

Table 3: List of the available sensors over several platforms, the number of accepted channels for the assimilation, and the percentage of assimilated observations calculated over all radiance observations and all cycles.

Sensor	Platform	Assimilated channels	Percentage over total
AIRS	AQUA	52	31.63 %
	NOAA15	2	3.31 %
AMSUA	NOAA18	2	4.45 %
	METOP-A	2	2.08 %
IASI	METOP-A	66	52.72 %
	METOP-B	68	3.47 %
MHS	NOAA19	2	0.68 %
	METOP-A	3	0.8 %
	METOP-B	3	0.85 %

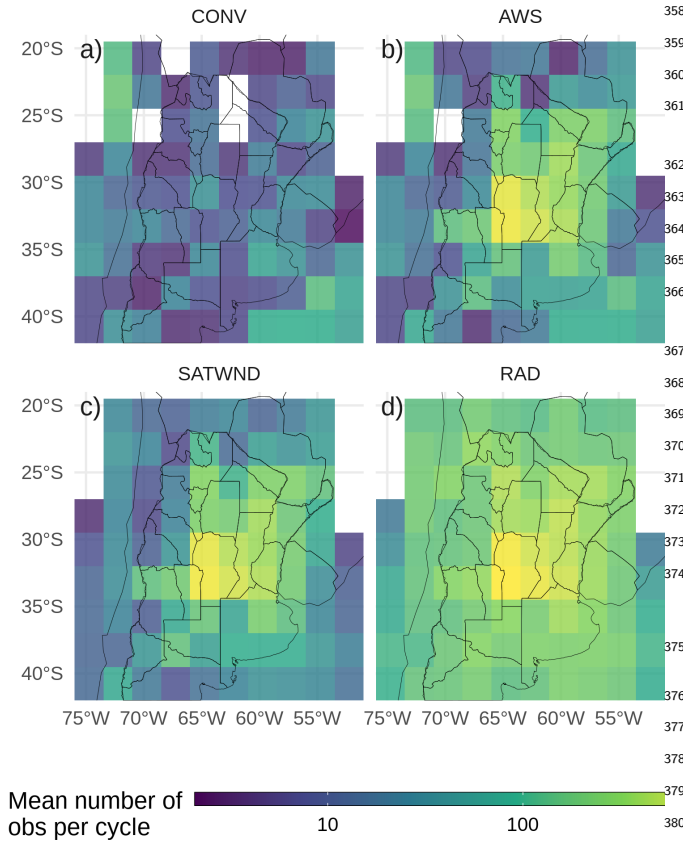


Figure 3: Horizontal spatial distribution of the mean available observations per analysis cycle for the a) CONV, b) AWS, c) SATWND, and d) RAD experiments calculated over 2.5° boxes.

Table 4: Observation types assimilated in each experiment.

Obs type	CONV	AWS	SATWND	RAD
Conventional (PREPBUFR)	x	x	x	x
Conventional (AWS)		x	x	x
Satellite-derived winds			x	x
Radiances				x

present [?]. The variables of interest (air temperature, humidity and wind) were interpolated to the model grid to compare them with the analysis of each experiment.

- The Multi-Network Composite Highest Resolution Radiosonde Data [Laboratory] from the RELAMPAGO field campaign database consisting of high-resolution radiosondes launched from several locations during the IOPs along with the operational radiosondes. Only the soundings that did not enter the assimilation system were used for validation. The experiment period covers IOP missions 7 and 8, during which 74 radiosondes were launched in a small area near the center of the experimental domain (Figure 2b).
- The Satellite precipitation estimation IMERG Final Run with 0.01° spatial resolution and 30 minutes temporal resolution [Huffman et al.] was used as a reference state to validate the skill of 1-hour forecasts to represent the precipitation over the domain.
- Radar observations are used to perform a qualitative and visual assessment of the convective features. The data comes from 9 radars located in the domain and is provided by the Argentine C-band Doppler dual-polarization weather radar network [de Elía et al.] with a temporal frequency of 10 minutes. For this work, only the maximum reflectivity in the column (COLMAX) closest to the analysis time was used.

2.4. Experimental design

To investigate the impact of different observations upon the analysis, four DA experiments were performed using different observation sets (Table 4). The CONV experiment uses only conventional observations from PREPBUFR. In a second experiment, referred to as AWS, we assimilate all the observations included in CONV plus the 10-minute frequency surface observations from AWS. In the third experiment, referred to as SATWND, we assimilate all the observations of the AWS experiment and the satellite-derived winds. Finally, a fourth experiment referred to as RAD assimilates all available clear-sky radiances from sensors onboard polar orbiting satellites as described in section 2.3.4.

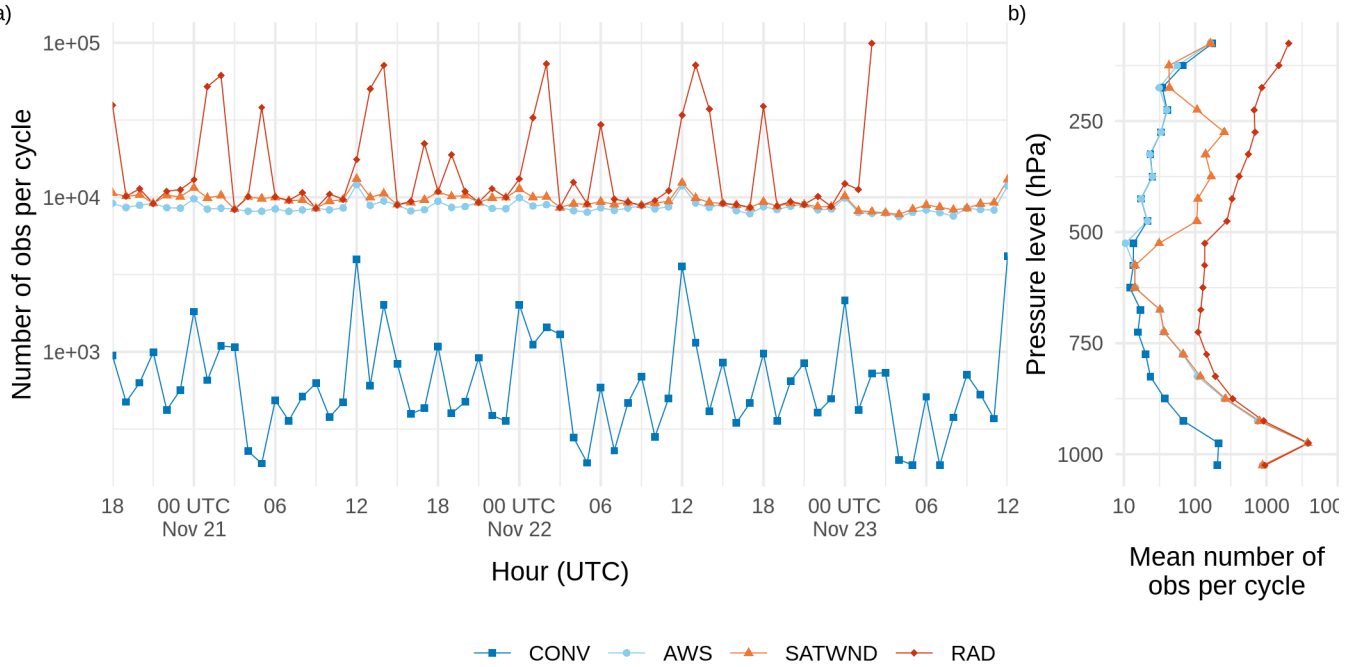


Figure 4: a) Number of assimilated observations per cycle and b) time averaged number of assimilated observations per cycle divided into 50 hPa-depth vertical layers for the CONV (blue squares and line), AWS (light blue dots and line), SATWND (orange triangles and line) and RAD (red diamonds and line) experiments.

389 The horizontal distribution of the average number of
 390 assimilated observations per cycle in each experiment is
 391 shown in Figure 3. The larger number of assimilated obser-
 392 vations over the center and east of the domain corresponds
 393 to the AWS observations. In Figure 4a the number of
 394 assimilated observations over time is shown. Local maxima
 395 at 12 and 00 UTC found mainly in CONV are attributed to
 396 operational soundings. The strong variability in the num-
 397 ber of radiance observations per cycle is also noticeable and
 398 depends on the satellite coverage. The maxima at 13-14
 399 and 01-02 UTC in RAD correspond to the contribution of
 400 the multispectral sensors. The vertical distribution of the
 401 mean number of observations per cycle (Figure 4b) shows
 402 a maximum in low levels due to the AWS observations.
 403 Satellite-derived winds are maximized at the upper tropo-
 404 sphere (between 500-250 hPa). Above 850 hPa, most of
 405 the observations correspond to radiance observations.

406 All the assimilation experiments start at 18 UTC Nov
 407 20, 2018 and continue until 12 UTC Nov, 23 (totaling 67
 408 hours/assimilation cycles). The initial 60-member ensemble
 409 is generated as explained in section 2.2 from a spin-up run
 410 without assimilating observations performed between 12
 411 UTC and 18 UTC Nov, 20 (Figure 5).

412 Ensemble forecasts initialized from the different analysis
 413 experiments at 00 and 06 UTC Nov 22 were performed
 414 to evaluate the impact of the different observing networks
 415 on short range precipitation forecasts. Both forecasts are
 416 integrated until 12 UTC Nov 23. All forecasts use the
 417 same domain and ensemble configuration as the analysis.
 418 The boundary conditions for the ensemble members are

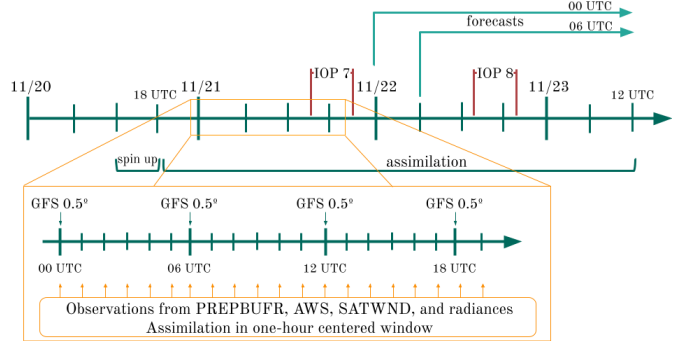


Figure 5: Diagram of the analysis cycles between 18 UTC Nov 20, and 12 UTC Nov 23 plus spin up period of 6 hours. The zoomed section shows the hourly assimilation that is performed within a one-hour centered window and new boundary conditions from GFS every 6 hours. The two IOP missions from the RELAMPAGO field campaign and the ensemble forecast initialized at 00 and 06 UTC Nov 22 are shown.

generated by adding random perturbations to the GFS deterministic forecast (0.25° horizontal grid spacing and 6-hour temporal resolution; National Centers for Environmental Prediction, National Weather Service, NOAA, U.S. Department of Commerce).

2.5. Verification methods

A set of metrics are selected to evaluate different aspects of the analysis obtained in the experiments conducted in this paper. These aspects include a validation of how

428 the uncertainty is quantified in the first-guess and in the
 429 analysis, and how different experiments fit an independent
 430 set of observations that are not assimilated.

431 To evaluate the statistical consistency of the uncertainty
 432 quantification in the ensemble system we use the Reduced
 433 Centered Random Variable (RCRV, Candille et al.) which
 434 is defined as:

$$435 \quad RCRV = \frac{x_o - m}{\sqrt{\sigma_o^2 + \sigma^2}} \quad (2) \quad 471$$

436 where x_o is a assimilated observation and its error σ_o , the
 437 ensemble mean of the analysis in observational space m , and
 438 the standard deviation σ of the ensemble. The average of
 439 $RCRV$ computed over all the realizations or analysis cycles,
 440 represents the bias of the ensemble mean with respect to
 441 the observations normalized by the estimated uncertainty:
 442

$$443 \quad meanRCRV = E[RCRV] \quad (3) \quad 479$$

444 The standard deviation of the $RCRV$ or $sdRCRV$ mea-
 445 sures the agreement of the ensemble spread and the ob-
 446 servational error with respect to the distance between the
 447 ensemble mean and the observations, and then the system-
 448 atic over- or under- dispersion of the ensemble:

$$449 \quad sdRCRV = \sqrt{\frac{M}{M-1} E[(RCRV - meanRCRV)^2]} \quad (4) \quad 486$$

450 where M is the ensemble size. A consistent system will
 451 have no bias ($meanRCRV = 0$) and a standard deviation
 452 equal to 1 ($sdRCRV = 1$). If the ensemble has a positive
 453 bias, $meanRCRV$ will be positive, on the opposite, if
 454 the ensemble has a negative bias, $meanRCRV$ will be
 455 negative. A $sdRCRV > 1$ indicates that the difference
 456 between the observations and the ensemble mean is greater
 457 than combined uncertainty of the observations and the
 458 model, hence, the ensemble is underdispersive. On the
 459 contrary, an $sdRCRV < 1$ will indicate that the ensemble
 460 is overdispersive [Candille et al.].

461 The fit of the first-guess and analysis to a set of in-
 462 dependent observations, the high-resolution radiosondes
 463 from RELAMPAGO, is computed based on the Root Mean
 464 Square Error (RMSE) and the BIAS:

$$465 \quad RMSE = \sqrt{\frac{1}{N} \sum_{i=1}^N (X_i - O_i)^2} \quad (5) \quad 505$$

$$466 \quad BIAS = \frac{1}{N} \sum_{i=1}^N (X_i - O_i) \quad (6) \quad 506$$

467 where O and X stand for independent observations and
 468 the simulations respectively, and N is the sample size.

469 For the comparison of the first-guess precipitation with
 470 the IMERG precipitation estimates, we compute the Frac-
 471 tions Skill Score (FSS, Roberts) for different neighborhood
 472 length scales and thresholds:

$$473 \quad FSS = 1 - \frac{\sum_{i=1}^N (P_{xi} - P_{oi})^2}{\sum_{i=1}^N (P_{xi})^2 + \sum_{i=1}^N (P_{oi})^2} \quad (7)$$

474 where P_{oi} is the fraction of grid points in the i -th
 475 sampling area in which the observed accumulated precipi-
 476 tation is greater than a specified threshold. Following
 477 Roberts et al., P_{xi} is calculated from the ensemble prob-
 478 ability precipitation over the same threshold in each grid
 479 point by averaging over the i -th sampling area. The FSS
 480 was computed from the accumulated precipitation over 6
 481 hr periods by adding the 1-hr accumulated precipitation
 482 forecasts over 6 consecutive assimilation cycles.

2.6. Computation procedures

We performed all the experiments at the National Center for Atmospheric Research (NCAR) supercomputer Cheyenne [Computational and Information Systems Laboratory]. All the analyses in this paper were performed using the R programming language [?], using data.table [?] and metR [?] packages. All graphics are made using ggplot2 [?] and the paper was rendered using knitr and rmarkdown [??].

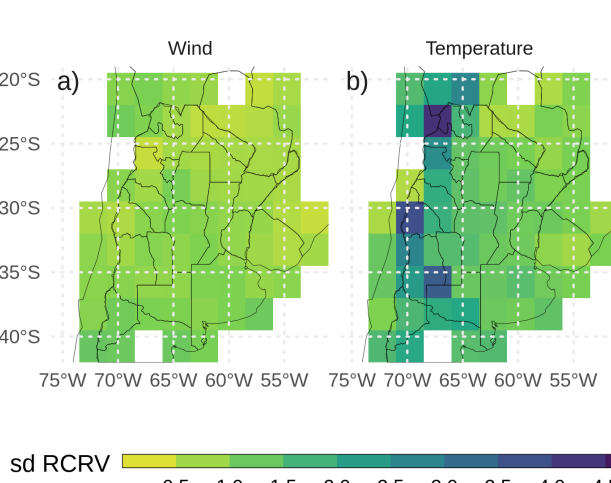
3. Results

3.1. Ensemble consistency

To investigate the ability of the first-guess ensemble mean to fit the observations taking into account the uncertainties of the forecast and the observations, we calculated the $meanRCRV$ and the $sdRCRV$ for the RAD experiment. As this experiment assimilates all types of observations used in this work, it is possible to analyze the consistency of the ensemble by comparing it with each type of observation. Figure 6 shows the $sdRCRV$ for surface observations box-averaged to a 2.5° grid. The $sdRCRV$ for wind observations (Figure 6a) is close to 1 suggesting a good agreement between the ensemble spread, the forecast error, and the observation error. For the temperature (Figure 6b), the results are similar except that for some areas in the west of the domain the $sdRCRV$ can be as high as 4.5. In this region, the mean innovation was overly large due to the complex terrain leading to large differences between the model topography and the station height.

Figure 7 shows the mean and standard deviation of the RCRV for the upper-air observations. Figures 7a-b show the RCRV statistics for soundings (ADPUPA) and aircraft (AIRCAR and AIRCFT). Both ADPUPA and AIRCFT show a generally good agreement between the ensemble spread and the observation error. As sounding observations and their associated errors are known to be reliable, this result indicates that the ensemble has an appropriate spread. AIRCAR presents an irregular profile with $sdRCRV$ values that suggest that the error for this type of observation is overestimated. ADPUPA and AIRCAR present a $meanRCRV$ profile near zero at middle and upper levels. At low levels, the $meanRCRV$ profile is positive,

545 3.2. Impacts of assimilated observations



567 Figure 6: First guess $sdRCRV$ calculated for surface observations₅₆₇
 568 (from PREPBUFR and AWS) of a) wind, and b) temperature aver-₅₆₈
 569 aged over 2.5° boxes for the RAD experiment. Observations were
 570 aggregated every hourly cycle for the entire experiment period.₅₆₉

517 showing a cold bias present in the model, a characteristic₅₇₂
 518 already studied in Ruiz et al. and Dillon et al. [b].₅₇₃

519 Satellite-derived winds observations varies in number₅₇₄
 520 depending on the satellite and the level. In Figure 7c we₅₇₅
 521 included the $RCRV$ calculated at least with 100 ob-₅₇₆
 522 servations for each satellite and level. At low levels, where₅₇₇
 523 there are not many observations available, the profiles of₅₇₈
 524 mean $RCRV$ and $sdRCRV$ show a larger departure from₅₇₉
 525 the expected behavior with a negative bias, and a possible₅₈₀
 526 overestimation of the observation error. Wind estimations₅₈₁
 527 derived from water vapor channels are abundant above 500₅₈₂
 528 hPa where their bias is close to zero. The only exception₅₈₃
 529 are the EUMETSAT observations which contribute very₅₈₄
 530 little in the region.₅₈₅

531 The mean $RCRV$ profiles calculated from the radiance₅₈₇
 532 observations (Figure 7d) show almost no bias and the₅₈₈
 533 same happens if the mean $RCRV$ is calculated over each₅₈₉
 534 channel of each sensor (not shown). This indicates that₅₉₀
 535 the bias correction algorithm works as expected. The₅₉₁
 536 $sdRCRV$ values are less than 1 for all sensors possibly due₅₉₂
 537 to an overestimation of the observation errors to reduce₅₉₃
 538 the influence of potentially erroneous observations.₅₉₄

539 Overall, these results indicate that the ensemble spread₅₉₅
 540 is consistent with the short-range forecast error and that₅₉₆
 541 systematic errors are relatively small for most of the ob-₅₉₇
 542 servation types used in this work. Moreover, these results₅₉₈
 543 suggest the relaxation-to-prior spread inflation inflation₅₉₉
 544 parameter $\alpha = 0.9$ is adequate for the system.₆₀₀

546 In this section, we present the impact of assimilating dif-
 547 ferent observation types on variables which are particularly
 548 relevant for the occurrence of deep moist convection. The
 549 analysis is performed over a smaller domain (red box in
 550 Figure 2a) to focus on the region most directly affected
 551 by the MCS. Figures 8a-c show the analysis difference be-
 552 tween experiments in the spatially averaged vertical profile
 553 of temperature. By averaging the differences between two
 554 experiments we can isolate the systematic impact produced
 555 by different observing systems on the analyzed state. Dur-
 556 ing the first day, the assimilation of AWS observations
 557 results in a colder PBL. This cooling effect has a clear
 558 diurnal cycle, being stronger during nighttime (Figure 8a).
 559 During the second day of the experiment, the impact of
 560 AWS observations extends into the middle and upper tro-
 561 posphere coinciding with the mature stage of the MCS.
 562 The warm difference shown in AWS-CONV between 500
 563 and 200 hPa is produced by the development of stronger
 564 convection in AWS compared to CONV. This is a good
 565 example of how low-level information provided by surface
 566 weather stations can rapidly spread into the troposphere
 567 in the presence of deep moist convection. Although the
 568 mid-to-upper circulation can have an important impact on
 569 the organization and evolution of the MCS over the region,
 570 the satellite-derived winds did not have an appreciable im-
 571 pact on the mean temperature and humidity (Figure 8b-e),
 572 possibly due to the large observation errors used for the
 573 assimilation. During the first day of the experiment, the
 574 assimilation of radiances produces a warming effect in the
 575 PBL which partially compensates for the cooling effect of
 576 AWS observations (Figure 8c). No clear systematic impact
 577 is found above the PBL during this period. During the
 578 second day, the impact of radiance observations is found
 579 through the troposphere with a distribution that is similar
 580 to the impact found in the AWS experiment but with the
 581 opposite sign.

582 Comparing the specific humidity in the experiments (Fig-
 583 ures 8d-f), the impact of assimilating AWS with fine spatial
 584 and temporal resolution is most substantial at low levels
 585 (Figure 8d). The PBL in the AWS experiment is consis-
 586 tently moister than in the CONV experiment particularly
 587 at nighttime. The increase in low-level moisture by a denser
 588 surface network is consistent with previously reported dry
 589 biases in the WRF model over the region [?, ?, Ruiz et al.].
 590 We found that the moistening of the PBL is mainly driven
 591 by the covariance between temperature and specific hu-
 592 midity within the PBL. In our experiment and over the
 593 center of the domain, this covariance remains negative,
 594 increasing low-level moisture as the observations introduce
 595 negative temperature corrections. As for the temperature,
 596 the systematic impact of satellite-derived winds on mois-
 597 ture is small (Figure 8e). Figure 8f shows that radiances
 598 reduce low-middle level moisture during the first day of
 599 the experiment. The drying effect extends to lower-middle
 600 levels during the second day of the experiment coinciding

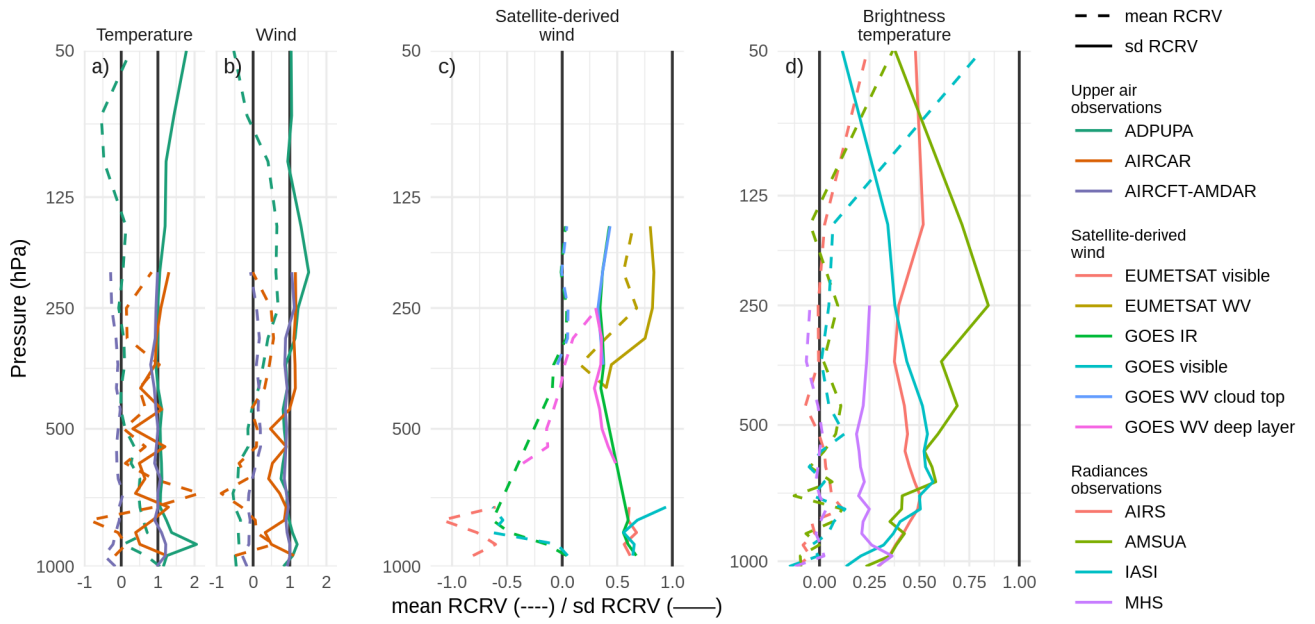


Figure 7: Vertical profiles of first guess *meanRCRV* (dashed line) and *sdRCRV* (solid line) for a) temperature and b) wind of sounding and aircraft observations, c) satellite-derived wind observations, and d) brightness temperature observations for the RAD experiment. Observations were aggregated every hourly cycle for the entire experiment period.

with the development of the MCS between 00 and 12 UTC Nov 22.

The impacts on the wind components are shown in Figure 9, along with the corresponding averaged wind component in the experiment with the largest number of assimilated observations (for example, Figure 9a shows the zonal wind difference between AWS and CONV and the zonal wind for AWS). The assimilation of AWS produces a more easterly wind and a less northerly wind at low levels during the first two days of analysis (Figures 9a,b). There is a diurnal cycle in the impact of surface weather stations on the meridional velocity (Figure 9d) with a stronger reduction of the northerly wind during night hours. This indicates that surface observations are reducing the intensity of the low-level jet present in the pre-convective environment. After 18 UTC Nov 22, the opposite effect is observed when the MCS is moving through the domain. After the initiation of the convective cells, the systematic impact on the wind field is larger at mid and upper levels (Figures 9d, f). During Nov 22 and 23 the impact of assimilating AWS observations produces an increase of northerly wind in upper levels. This could be a consequence of a stronger MCS with an increased polar side upper level outflow. Although satellite-derived wind observations produce the largest impact in mid-to-upper levels where the number of observations is largest; the systematic impact is overall smaller than the one produced by assimilating data from AWS (Figures 9b, e). The reason of the small impact observed in SATWND could be associated to the large observation error used for satellite-derived wind observations.

The assimilation of radiances produces a reduction in the westerly wind compared with respect to SATWIND in low and upper levels (Figure 9c). For the meridional wind, these observations produce an enhancement on average of the northerly low-level flow of 1ms^{-1} , opposite to what is generated by the assimilation of AWS observations during the nights, between 03 and 12 UTC, previous to the development of the MCS (Figure 9f). At upper levels and during Nov 22 and 23 the average impact of assimilating radiances is a decrease in the wind speed. The meridional wind field at 200 hPa at different times shows that the outflow from the MCS is even more intense than in the other experiments, while the southerly wind ahead of the MCS also increases producing an average reduction of the northerly wind (Figure 9f).

We also compared ensemble mean analyses to ERA5 reanalyses (reference), which corroborates Figs. 7 and 8. Specifically, Moreover, these adjustments due to assimilating radiance/AWS observations lead to ensemble mean analyses closer to ERA5 reanalyses".

To investigate how changes in the PBL can modify the pre-convective environment, we compare the horizontal distribution of the low level northerly flow (for the first 7 sigma levels), precipitable water, low level temperature, and CAPE for the analysis at 00 UTC Nov 22 (after 30 assimilation cycles). At that moment the first convective cells were developing over the southern region of the domain along the cold front. Figure 11a shows the precipitable water (shaded) and the vertically averaged low-level meridional wind component (contours). We found that the moist

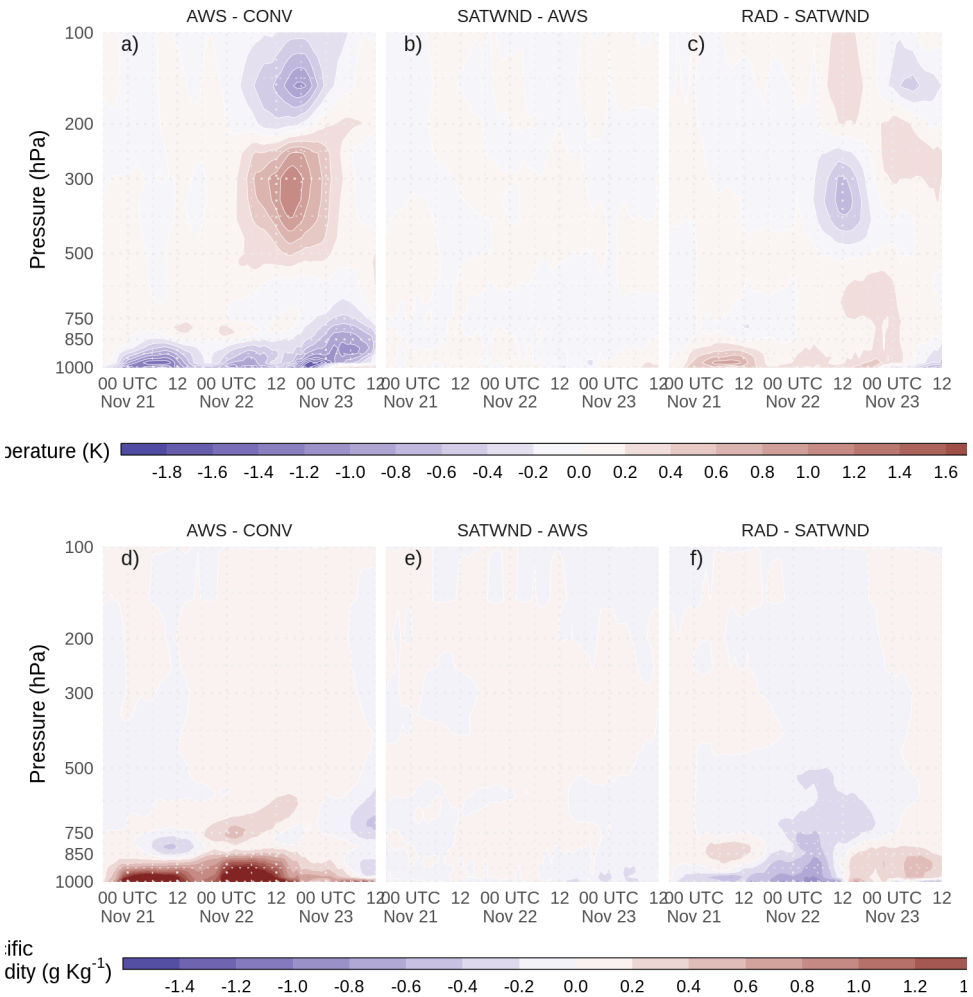


Figure 8: Difference between analysis ensemble mean experiments a) and d) AWS-CONV, b) and e) SATWND-AWS, and c) and f) RAD-SATWND for the spatially averaged vertical profiles of temperature (a, b, and c, in K) and specific humidity (d, e, and f in $g\ kg^{-1}$) calculated over the inner domain (red box in Figure 2a) for each analysis cycle.

tongue extending over the northern part of the domain is⁶⁷⁹ enhanced by the assimilation of denser surface observations⁶⁸⁰. The moisture increase is particularly strong at the southern⁶⁸¹ tip of this tongue, just ahead of the cold front where con-⁶⁸²vection initiation was taking place. AWS and SATWND⁶⁸³ experiments are very similar, with values of precipitable⁶⁸⁴ water over $55\ kgm^{-2}$ north of $30^{\circ}S$ and a similar vertical⁶⁸⁵ distribution of specific humidity (not shown). RAD has⁶⁸⁶ lower precipitable water content than AWS and SATWND,⁶⁸⁷ but higher than CONV. The distribution of moisture at low⁶⁸⁸ levels in RAD seems to be the result of the combination of⁶⁸⁹ the moistening effect of assimilating AWS – partially com-⁶⁹⁰pensated by the assimilation of radiance observations – and⁶⁹¹ a reduced meridional moisture transport due to the weaker⁶⁹² northerly flow over the center of the domain compared to⁶⁹³ CONV.⁶⁹⁴

The analyzed distribution of temperature and moisture⁶⁹⁵ in the PBL (Figure 11b) resembles the characteristics ob-

served in the temperature profiles (Figure 8a-c) where AWS produces a colder PBL than CONV while the PBL in RAD is warmer than in SATWND. On average the PBL in AWS and SATWND is colder than in CONV, while RAD shows a warmer PBL than AWS due to the assimilation of radiance observations. Figure 11c shows the most unstable convective available potential energy (MCAPE, shaded) and the 0 to 6 km wind shear. The values of MCAPE in CONV do not exceed $2000\ J\ Kg^{-1}$ while the rest of the experiments show maximum MCAPE over $4000\ J\ Kg^{-1}$. MCAPE in the RAD experiment is lower compared to AWS or SATWND. This is consistent with less humidity in the PBL with respect to these experiments but may be partially compensated by a slightly warmer PBL in the RAD experiment. The 0-6 km wind shear is more intense in AWS, SATWND, and RAD reaching values over $15\ m\ s^{-1}$ at the southern tip of the region with positive MCAPE values. Moreover, in this same region, these experiments

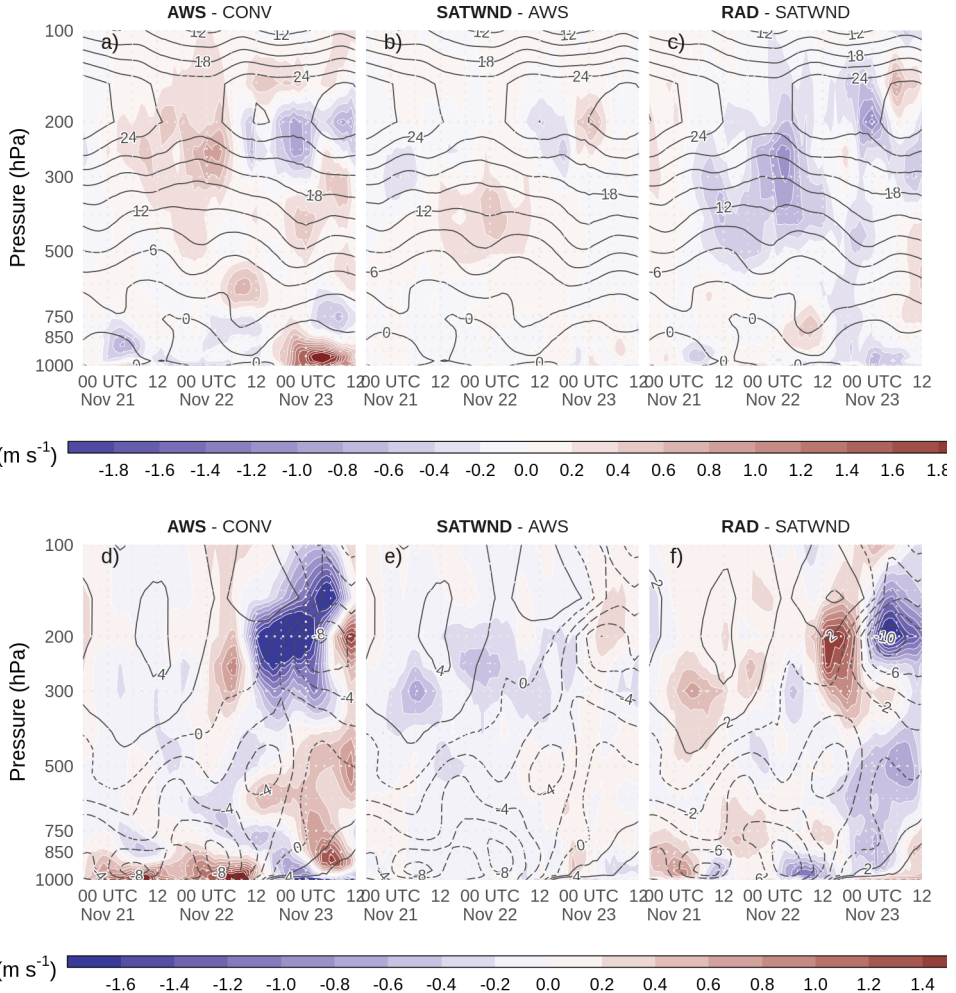


Figure 9: Difference between analysis ensemble mean experiments a) and d) AWS-CONV, b) and e) SATWND-AWS, and c) and f) RAD-SATWND for the spatially averaged vertical profiles of u wind (a, b, and c, in $m s^{-1}$) and v wind (d, e, and f in $m s^{-1}$) calculated over the inner domain (red box in Figure 2a) for each analysis cycle. Black contours correspond to u wind and dashed contours to negative v wind for (a) AWS, (b) SATWND, and (c) RAD and v wind for (d) AWS, (e) SATWND, and (f) RAD since those experiments are the ones with more assimilated observations in each panel.

show larger MCAPE values than CONV. Note that wind shear over $15 m s^{-1}$ is associated with the development of more intense and organized MCSs [Chen et al., a] and also with conditions favorable for supercells [Markowski and Richardson].

3.3. Validation against independent observations

First, we analyze the impact of assimilating different observation types in terms of the representation of the MCS and its associated precipitation. Figure 12a shows the hourly accumulated precipitation as estimated by IMERG, and the probability matched mean (PM) [Clark] for the first-guess hourly accumulated precipitation as averaged between 67°W and 54.5°W as a function of time and latitude in the different experiments. The heaviest precipitation (over $12 mmh^{-1}$) starts during the afternoon of Nov 22 and

continues during Nov 23 after the end of the simulated period (Figure 12a). In all the experiments, the accumulated precipitation in the short-range forecasts is underestimated. This is particularly evident in CONV (Figure 12b), where the convection initiation is delayed and occurs further north with respect to the observed initiation. AWS, SATWND, and RAD better capture the timing and location of convective initiation (Figures 12c-e). AWS and RAD show a more fragmented distribution compared with SATWND, possibly due to the development of less organized convection during Nov 22. After 18 UTC Nov 22, RAD shows improvements in the precipitation rate and its distribution compared to the other experiments as a result of enhanced development of the convection.

We computed the FSS to quantify the spatial match between the observed precipitation and the first-guess hourly accumulated precipitation for the different experiments

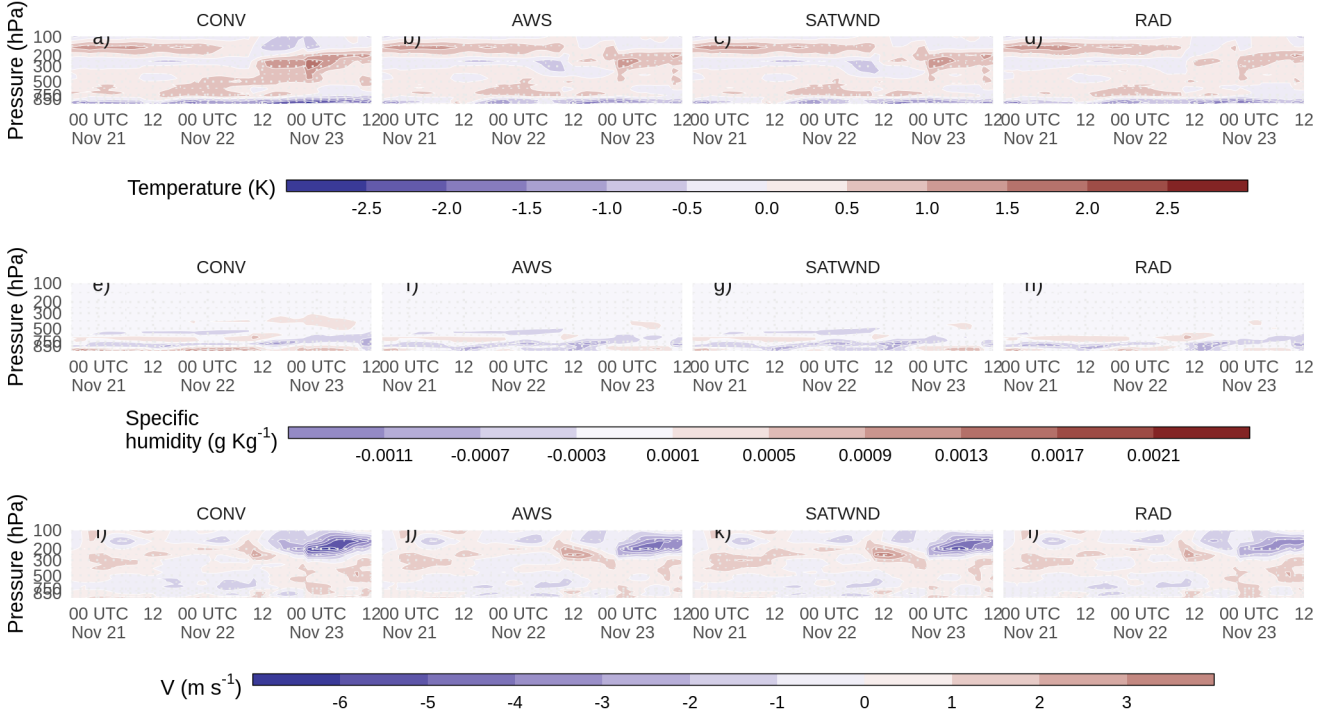


Figure 10: Difference between analysis ensemble mean experiments and ERA5 for the spatially averaged vertical profiles of air temperature (K, a-d), specific humidity ($g\text{ Kg}^{-1}$, e-h) and meridional wind ($m\text{ s}^{-1}$, i-l) calculated over the inner domain (red box in Figure 2a) for each analysis cycle.

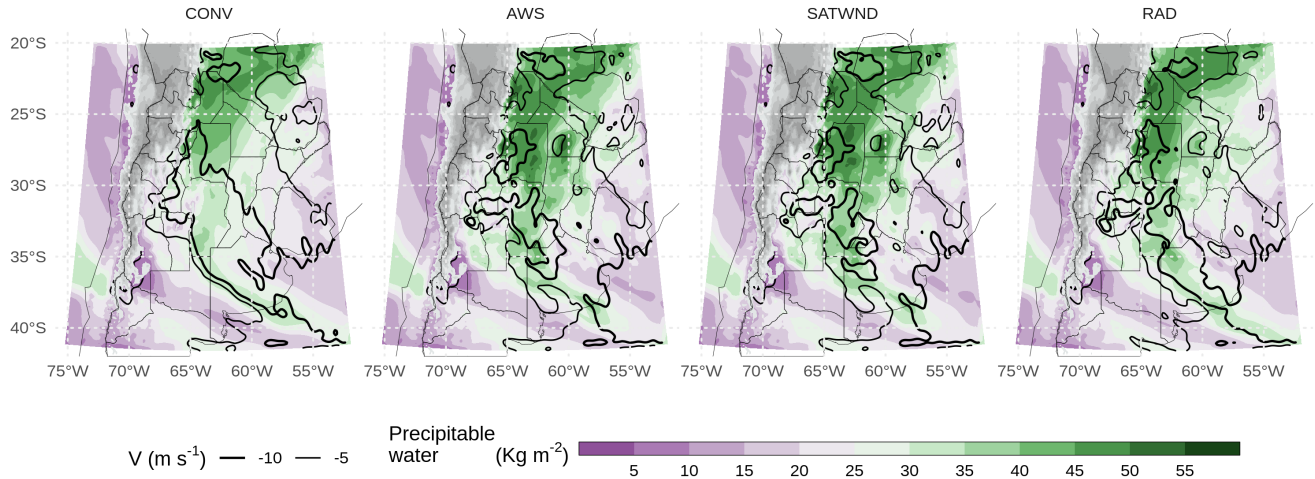
(Figure 13). For each threshold and spatial scale, we applied Equation @red(eq: eq7) in 6-hours rolling windows throughout the experiment period. All experiments show similar values of FSS during the initiation of the convection before 06 UTC Nov 22 except for RAD which performs better than the rest of the experiments during this period. This indicates that radiance observations have a positive impact on the analysis. The FSS for CONV is the lowest compared to the rest of the experiments and the differences are larger during the mature stage of the MCS. AWS and SATWND show similar FSSs indicating that satellite-derived wind assimilation has little impact on the precipitation for this case study. The assimilation of radiances led to an overall improvement of the 1-hour forecast precipitation, particularly for the 25 mm threshold during the period of heaviest precipitation on Nov 22 (Figure 13b,d). The enhancement is also important at the developing stage of the MCS (between 00 and 12 UTC Nov 22 and also for spatial scales above 500 km, not shown).

To complement the analysis, Figure 14 shows the observed maximum reflectivity in the vertical column (COLMAX) and the ensemble mean COLMAX for the CONV and RAD experiments at different times between 10 and 19 UTC Nov 22. These experiments were chosen because they represent the analysis with the minimum (CONV) and maximum (RAD) number of assimilated observations. In addition, they are the worst (CONV) and best (RAD)

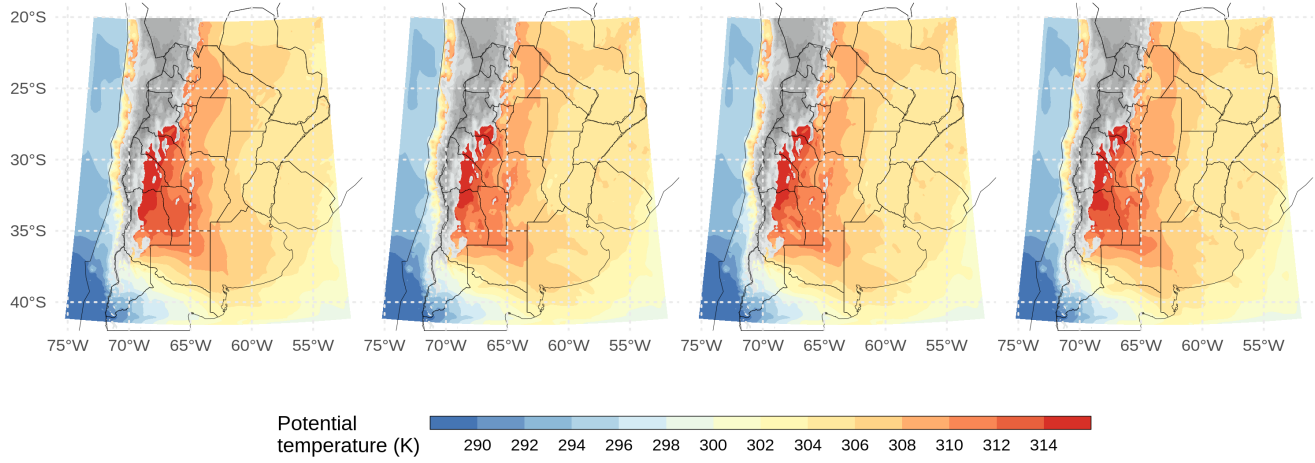
performing experiments in terms of the 1-hour precipitation forecast skill (Figure 13). Overall, none of the short-range forecasts capture the mesoscale details in the reflectivity distribution. This is partially expected considering the coarse horizontal grid spacing (10 km), which is not enough to appropriately represent the strength of the convective band associated with the MCS. Also, the ensemble mean produces a smoothing effect that reduces the amplitude of local maxima in the forecast reflectivity field. RAD better represents the observed features of the system showing a stronger and more organized MCS than CONV, over the domain center at 10 and 13 UTC (first and second columns in Figure 14). The convective cells that initiate after 16 UTC along the warm front in the northeast part of the domain are well captured by both experiments but are better represented in terms of strength in RAD. In addition, CONV captures the location of the MCS, but the convection seems to be less organized and much weaker than in RAD. Before and after the times shown in Figure 14, the agreement between location of the observed convective cells and the simulated in the experiment is quite good in the regions where radar data are available, especially for RAD.

Finally, Figure 15 shows the RMSE and bias calculated by comparing the experiments with radiosonde data from the RELAMPAGO missions, IOP 7 from 15 to 21 UTC Nov 21 (including 30 radiosondes), and IOP 8 from 14 to 20 UTC Nov 22 (including 22 radiosondes).

a)



b)



c)

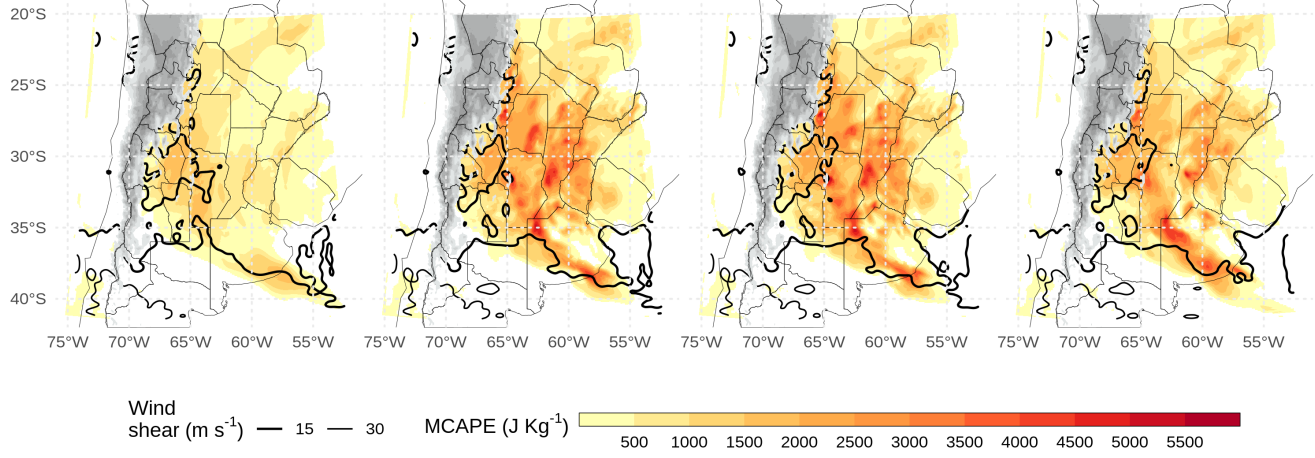


Figure 11: a) Precipitable water (shaded, kg m^{-2}) and average northerly wind over the first 7 sigma levels (from the surface up to approximately 800 hPa, contours, m s^{-1}), b) Average potential temperature for the PBL (first 10 sigma levels), and c) Maximum CAPE and $\sim 0\text{-}6$ km wind shear over 15 and 30 m s^{-1} for each experiment. All fields correspond to the analysis ensemble mean for 00 UTC Nov 22. Grey filled contours correspond to topography over 1500 meters above sea level.

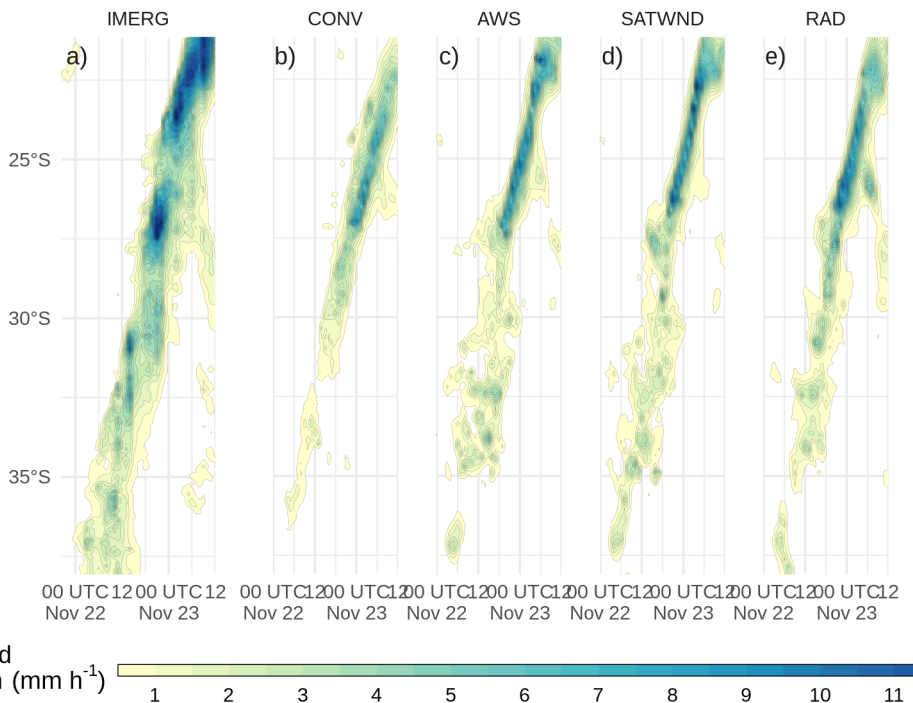


Figure 12: Hövmoller diagram of probability matched mean hourly accumulated 1-h forecast precipitation for each latitude band estimated by IMERG (left) and simulated (right), for the ensemble mean of each experiment, averaged over a longitude range between 67°W and 54.5°W . Contours drawn every 0.5 mm h^{-1} , starting at 0.5 mm h^{-1} .

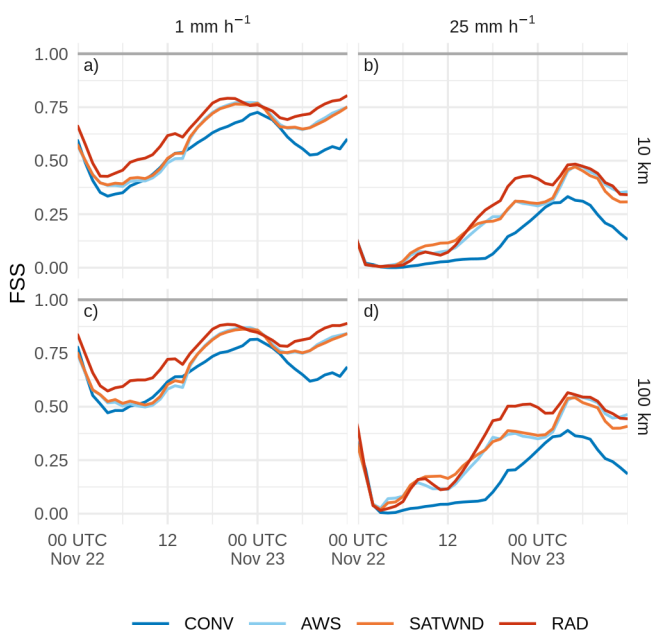


Figure 13: FSS calculated over 1-h forecast precipitation accumulated in a 6-hour moving window for 1 mm h^{-1} (a and c) and 25 mm h^{-1} (b and d) thresholds, on 10 km (a and b) and 100 km (c and d) scales, for the first-guess of CONV (blue line), AWS (light blue line), SATWND (orange line) and RAD (red line) experiments.

IOP 7 (Figures 15a-d) provides a good characterization of the pre-convective environment during the first day of our experiments. The area where the observations were taken was characterized by mostly clear skies and a low-level northerly flow associated with warm and moist advection. In general, the experiments show a similar RMSE and bias for all the variables. AWS observations were able to reduce the RMSE for temperature and dew point temperature in the PBL and reduce a small dry bias. However, AWS increments (Figure @red(fig:UV-diff)d) degraded the zonal wind between 7 and 12 km increasing the bias and RMSE (Figure 15c).

For IOP 8 (Figures 15e-h), the densely observed area was behind the MCS, but far enough from it to not be directly affected by its mesoscale circulation. This area was also behind the cold front and affected by low-level cold advection. The assimilation of AWS, SATWND, and RAD reduces the cold bias and RMSE for temperature between 5 and 12 km and the RMSE in the PBL compared with CONV (Figure 15e). The reduction of bias and RMSE is also important for dew point temperature (Figure 15f) with SATWND showing the biggest impact followed by AWS and RAD. The zonal wind is overestimated in the analyses and only RAD shows an improvement with respect to CONV in the upper troposphere (Figure 15g). At low levels the meridional wind (Figure 15g) presents a negative bias, indicating an underestimation of the southerly wind behind

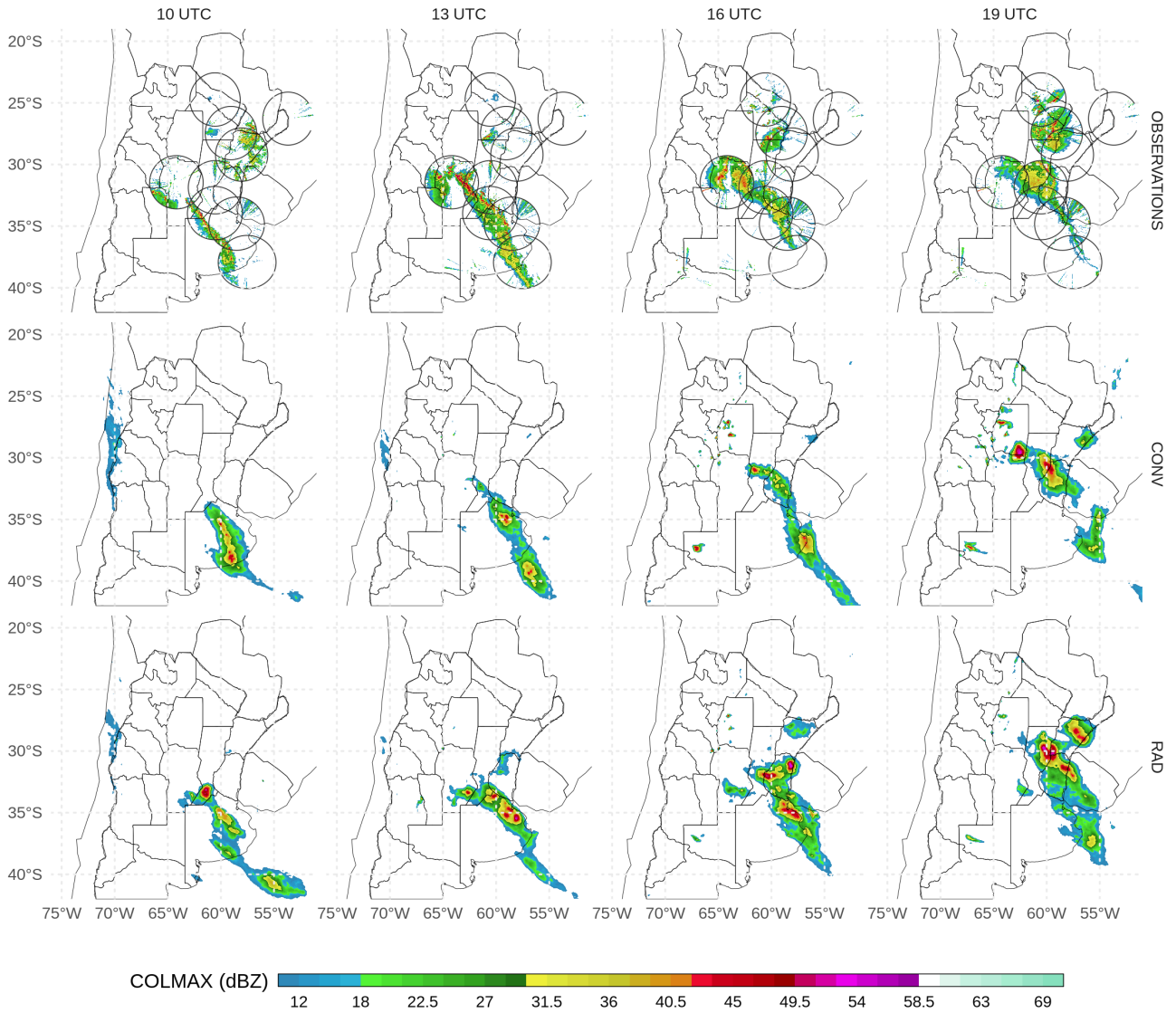


Figure 14: Maximum reflectivity in the column (COLMAX in dBZ), observed (upper row) and 1-hr forecast probability matched mean column maximum reflectivity for CONV (second row) and RAD (third row) at 10 UTC (first column), 13 UTC (second column), 16 UTC (third column), and 19 UTC (fourth column) Nov 22, 2018. Black circles in first row show the observation range of each radar.

the cold front principally in AWS, SATWND, and RAD.
In fact, low level biases in these experiments are higher
than in the CONV experiment, indicating a detrimental
effect of the additional observations (possibly associated
with the effect of AWS).

3.4. Ensemble forecast validation

In this section, we analyze the 60-member ensemble forecast initialized at 00 and 06 UTC Nov 22 from each experiment that runs for 36 and 30 h respectively, until 12 UTC Nov 23. We calculated the FSS for the ensemble forecasts in 6-hour rolling windows for the same thresholds and spatial scales as for the first-guess hourly accumulated precipitation to quantify the skill of the forecasts to predict precipitation (Figure 16). CONV forecasts perform

very poorly in terms of the FSS compared with the experiments that include other sources of observations. AWS, SATWND, and RAD show improvements in the FSS values, particularly for the higher threshold (Figure 16b, d). Moreover, the late initialization at 06 UTC performs better for AWS, SATWND, and RAD than the forecast initialized at 00 UTC, highlighting the positive impact of the observations assimilated between 00 and 06 UTC.

The satellite-derived wind observations show a clearly positive impact on the forecast, in contrast to what was seen when comparing the 1-h forecast with independent observations in terms of precipitation. Conversely, the radiance observations resulted in a neutral to a slightly negative impact on the forecast as opposed to what was seen when comparing the 1-h forecast to IMERG estimations.

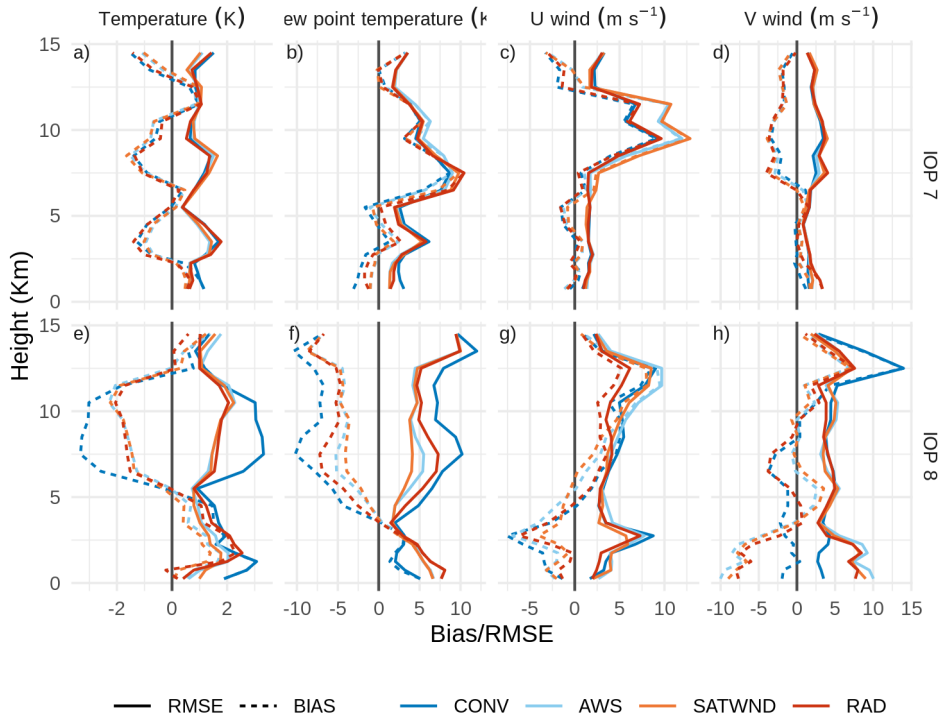


Figure 15: RMSE (solid line) and Bias (dashed line) of a) temperature (K), b) dew point temperature (K), c) u wind ($m s^{-1}$) and d) v wind ($m s^{-1}$) calculated by comparing the analysis of each experiment with the RELAMPAGO soundings during IOP 7 and IOP 8. The blue line corresponds to CONV, the light blue line to AWS, SATWND is represented with an orange line, and RAD with a red line.

839 The reason for why the forecasts initialized from RAD
 840 degrades over time needs to be further study.

841 4. Conclusions

842 In this paper, we investigate for the first time in South
 843 America the impact of different observation systems on the
 844 performance of an ensemble-based mesoscale regional DA
 845 system. In particular, we explore the impact upon the anal-
 846 ysis quality of assimilating frequent and relatively dense
 847 surface observations, satellite derived winds, and satellite
 848 clear-sky radiances from multiple sensors. Southern South
 849 America is a particularly interesting region due to the
 850 heterogeneity in topography and weather and sometimes
 851 coarse resolution of the operational observing network (con-
 852 sidering both surface based and upper air observations).
 853 This combined with a climatology characterized by frequent
 854 organized convective events makes mesoscale DA partic-
 855 ularly challenging. To consider these issues, we used a case
 856 study approach of a massive mesoscale convective system
 857 that developed over Southern South America, particularly
 858 in a region where the surface and upper-air observing net-
 859 works are too coarse to capture variability at the mesoscale
 860 and that took place on Nov 22, 2018.

861 We evaluated the consistency of the ensemble using the
 862 RCRV calculated for each type of observation used in RAD.
 863 Conventional observations including surface data and up-
 864 per air observations from soundings and aircraft, show a

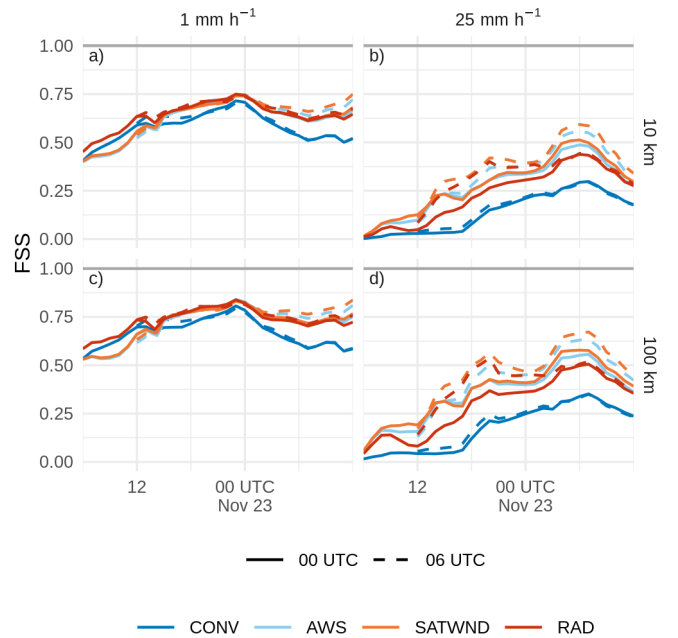


Figure 16: FSS calculated over a 6-hour moving window for 1 mm (a and c) and 25 mm (b and d) thresholds, on 10 km (a and b) and 100 km (c and d) scales, for the forecasts initialized from CONV (blue line), AWS (light blue line), SATWND (orange line), and RAD (red line) experiments at 00 UTC (solid line) and 06 UTC (dashed line), Nov 22.

865 $sdRCRV$ near 1 indicating a good agreement between the⁹²²
866 ensemble spread and the observational errors with respect⁹²³
867 to the distance between the ensemble mean and the observa⁹²⁴
868 tions. For satellite-derived winds and radiance observations⁹²⁵
869 the $sdRCRV$ is lower than 1, which could be the result of⁹²⁶
870 an underdispersive ensemble or an overestimation of the⁹²⁷
871 observation errors. However, taking into account that the⁹²⁸
872 observation error for satellite-derived wind is overestimated⁹²⁹
873 (to avoid strong impacts on the analysis for poor quality⁹³⁰
874 estimations) and that the results obtained for more reliable⁹³¹
875 observations (such as soundings) were good, we conclude⁹³²
876 that the ensemble has a reasonable spread.⁹³³

877 In terms of the analysis, we found that AWS observations⁹³⁴
878 which have high spatial and temporal resolution, produce⁹³⁵
879 impacts throughout the troposphere, especially in the PBL⁹³⁶
880 In particular, the precipitable water content and the low⁹³⁷
881 level meridional circulation in the AWS experiment lead to⁹³⁸
882 the development of deep convection and heavy precipitation⁹³⁹
883 closer to the observed in this case study. We also found
884 positive results when assimilating radiance observations⁹⁴⁰
885 that produce an adequate development of the convection,
886 mainly during the mature stage of the MCS, leading to⁹⁴¹
887 an increase in the accumulated precipitation compared⁹⁴²
888 with the other experiments. However, all experiments un-⁹⁴³
889 derestimated the 1-hour accumulated precipitation when⁹⁴⁴
890 compared to IMERG estimates. While the assimilation of⁹⁴⁵
891 satellite-derived wind does not produce a noticeable impact⁹⁴⁶
892 on the analysis with respect to the AWS experiment, this
893 is possibly due to the small number of observations in low⁹⁴⁷
894 levels available for this case study and its large observation
895 error. However, there are substantial improvements for the⁹⁴⁸
896 accumulated precipitation distribution. A more compre-⁹⁴⁹
897 hensive analysis is necessary to assess the possible impacts⁹⁵⁰
898 on middle and upper levels.⁹⁵¹

899 Taking advantage of the observations taken during the⁹⁵²
900 RELAMPAGO field campaign, we compared the experi-⁹⁵³
901 ments with the soundings launched during IOPs 7 and 8⁹⁵⁴
902 For the pre-convective environment (IOP 7), we observed⁹⁵⁵
903 an improvement at low levels when assimilating AWS obser-⁹⁵⁶
904 vations for the temperature, dew point temperature, and⁹⁵⁷
905 meridional wind. In particular, AWS observations correct⁹⁵⁸
906 a dry bias already observed by Ruiz et al.. For IOP 8,⁹⁵⁹
907 after the MCS crossed the center of the domain, we found⁹⁶⁰
908 a positive impact in low levels when assimilating more⁹⁶¹
909 observations for the temperature but the opposite effect for⁹⁶²
910 the dew point temperature. In this case, the analyses have⁹⁶³
911 a moist bias that increases with the assimilation of AWS
912 and radiance observations. We noted a negative covariance⁹⁶⁴
913 between temperature and moisture content over this region
914 that could lead to a moistening of the PBL. It is not clear⁹⁶⁵
915 what produces these negative covariances but it is evident⁹⁶⁶
916 that the corrections introduced by the observations are⁹⁶⁷
917 degrading the estimation of the moisture content during⁹⁶⁸
918 this period, which requires further analysis.⁹⁷⁰

919 We also analyzed the performance of independent ensem-⁹⁷¹
920 ble forecasts initialized from the analyses to forecast the⁹⁷²
921 precipitation during Nov 22. The forecast initialized from⁹⁷⁴

AWS, SATWND, and RAD are able to forecast the precipitation substantially better than CONV. In particular, the continuous assimilation of satellite-derived wind and radiance observations helps to improve the latest initialization but only the satellite-derived wind observations produces a positive impact that persists throughout the forecast.

To summarize, in this study we conclude that the assimilation of surface observations with high spatial and temporal resolution, satellite-derived winds, and clear-sky radiances from polar orbiting satellites had an overall positive impact on the development of the studied MCS and its associated precipitation. Moreover, the ensemble forecasts initialized from the analysis show promising results to predict the precipitation of severe events. In the future, we will further analyze the impacts in the independent forecasts and evaluate the implementation of other sources of observations like GPS radio occultation data and radiances from geostationary orbiting satellites like GOES-16.

5. Code and data availability

A version-controlled repository of the code used to create this analysis, including the code used to download the data can be found at <https://github.com/paocorralles/mesoda>. The derived data that support the findings of this study are also openly available in Zenodo at <http://doi.org/10.5072/zenodo.1060834>, version 0.9.0.

Acknowledgements

We are very thankful to the Atmospheric and Sea Research Center (CIMA), the University of Buenos Aires (UBA), and the National Scientific and Technical Research Council (CONICET) who support this study. We acknowledge the Sistema Nacional de Radares Meteorológicos supported by the Secretaría de Infraestructura y Política Hídrica for kindly providing the radar observations used for validation and the National Meteorological Service for facilitating the access to the data. We also acknowledge the Cheyenne HPC resources (doi:10.5065/D6RX99HX) from NCAR's Computational and Information Systems Laboratory, National Science Foundation (project code UIUC0012). Also, PICT 2017-2233 and PICT 2018-3202 projects of the National Agency for the Promotion of Research, Technological Development and Innovation from Argentina partially funded this project.

References

- Jeong-Ho Bae and Ki-Hong Min. Forecast Characteristics of Radar Data Assimilation Based on the Scales of Precipitation Systems. 14(3):605. ISSN 2072-4292. doi: 10.3390/rs14030605. URL <https://www.mdpi.com/2072-4292/14/3/605>.
- Ivette H. Banos, Will D. Mayfield, Guoqing Ge, Luiz F. Sapucci, Jacob R. Carley, and Louisa Nance. Assessment of the data assimilation framework for the Rapid Refresh Forecast System v0.1 and impacts on forecasts of convective storms. pages 1–36. ISSN 1991-959X. doi: 10.5194/gmd-2021-289. URL <https://gmd.copernicus.org/preprints/gmd-2021-289/>.

- Y. Bao, J. Xu, A. M. Powell Jr., M. Shao, J. Min, and Y. Pan. Impacts of AMSU-A, MHS and IASI data assimilation on temperature and humidity forecasts with GSI-WRF over the western United States. *8(10):4231–4242*. ISSN 1867-8548. doi: 10.5194/amt-8-4231-2015. URL <https://www.atmos-meas-tech.net/8/4231/2015/>.
- Harold E Brooks, James W Lee, and Jeffrey P Craven. The spatial distribution of severe thunderstorm and tornado environments from global reanalysis data. *67–68:73–94*. ISSN 01698095. doi: 10.1016/S0169-8095(03)00045-0. URL <https://linkinghub.elsevier.com/retrieve/pii/S0169809503000450>.
- G. Candille, C. Côté, P. L. Houtekamer, and G. Pellerin. Verification of an Ensemble Prediction System against Observations. *135(7):2688–2699*. ISSN 0027-0644, 1520-0493. doi: 10.1175/MWR3414.hss. URL <http://journals.ametsoc.org/doi/10.1175/MWR3414.1>.
- Daniel J. Cecil and Clay B. Blankenship. Toward a Global Climatology of Severe Hailstorms as Estimated by Satellite Passive Microwave Imagers. *25(2):687–703*. ISSN 0894-8755, 1520-0442. doi: 10.1175/JCLI-D-11-00130.1. URL <https://journals.ametsoc.org/view/journals/clim/25/2/jcli-d-11-00130.1.xml>.
- Weiguang Chang, Dominik Jacques, Luc Fillion, and Seung-Jong Baek. Assimilation of Hourly Surface Observations with the Canadian High-Resolution Ensemble Kalman Filter. *55(4-5):247–263*. ISSN 0705-5900. doi: 10.1080/07055900.2017.1384361. URL <https://doi.org/10.1080/07055900.2017.1384361>.
- Fei Chen and Jimy Dudhia. Coupling an Advanced Land Surface-Hydrology Model with the Penn State-NCAR MM5 Modeling System. Part I: Model Implementation and Sensitivity. *129(4):569–585*. ISSN 1520-0493, 0027-0644. doi: 10.1175/1520-0493(2001)129<0569:CAALSH>2.0.CO;2. URL https://journals.ametsoc.org/view/journals/mwre/129/4/1520-0493_2001_129_0569_caalsh_2.0.co_2.xml.
- Qian Chen, Jiwen Fan, Samson Hagos, William I. Gustafson, and Larry K. Berg. Roles of wind shear at different vertical levels on Cloud system organization and properties. *120(13):6551–6574*. ISSN 2169-8996. doi: 10.1002/2015JD023253. URL <https://agupubs.onlinelibrary.wiley.com/doi/abs/10.1002/2015JD023253>.
- Kingchao Chen, Kun Zhao, Juanzhen Sun, Bowen Zhou, and Wen-Chau Lee. Assimilating surface observations in a four-dimensional variational Doppler radar data assimilation system to improve analysis and forecast of a squall line case. *33(10):1106–1119*. ISSN 0256-1530, 1861-9533. doi: 10.1007/s00376-016-5290-0. URL <https://link.springer.com/10.1007/s00376-016-5290-0>.
- T. Cherubini, S. Businger, C. Velden, and R. Ogasawara. The Impacts of Satellite-Derived Atmospheric Motion Vectors on Mesoscale Forecasts over Hawaii. *134(7):2009–2020*. ISSN 1520-0493, 0027-0644. doi: 10.1175/MWR3163.1. URL <https://journals.ametsoc.org/view/journals/mwre/134/7/mwr3163.1.xml>.
- Adam J. Clark. Generation of Ensemble Mean Precipitation Forecasts from Convection-Allowing Ensembles. *32(4):1569–1583*. ISSN 1520-0434, 0882-8156. doi: 10.1175/WAF-D-16-0199. URL https://journals.ametsoc.org/view/journals/wefo/32/4/waf-d-16-0199_1.xml.
- Computational and Information Systems Laboratory. Cheyenne HPE/SGI ICE XA System (University Community Computing). doi: doi:10.5065/D6RX99HX.
- Ramón de Elía, Luciano Vidal, and Pedro Lohigorry. El smn y la red argentina de radares meteorológicos. URL <http://hdl.handle.net/20.500.12160/625>.
- María E. Dillon, Yanina García Skabar, Juan Ruiz, Eugenia Kalnay, Estela A. Collini, Pablo Echevarría, Marcos Saucedo, Takemasa Miyoshi, and Masaru Kunii. Application of the WRF-LETKF Data Assimilation System over Southern South America: Sensitivity to Model Physics. *31(1):217–236*, a. ISSN 0882-8156, 1520-0434. doi: 10.1175/WAF-D-14-00157.1. URL <http://journals.ametsoc.org/doi/10.1175/WAF-D-14-00157.1>.
- María Eugenia Dillon, Paula Maldonado, Paola Corrales, Yanina García Skabar, Juan Ruiz, Maximiliano Sacco, Federico Cutraro, Leonardo Mingari, Cynthia Matsudo, Luciano Vidal, Martín Rugna, María Paula Hobouchian, Paola Salio, Stephen Nesbitt, Celeste Saulo, Eugenia Kalnay, and Takemasa Miyoshi. A rapid refresh ensemble based data assimilation and forecast system for the RELAMPAGO field campaign. page 105858, b. ISSN 0169-8095. doi: 10.1016/j.atmosres.2021.105858. URL <https://www.sciencedirect.com/science/article/pii/S0169809521004142>.
- J. R. Eyre, S. J. English, and M. Forsythe. Assimilation of satellite data in numerical weather prediction. Part I: The early years. *146(726):49–68*. ISSN 1477-870X. doi: 10.1002/qj.3654. URL <https://onlinelibrary.wiley.com/doi/abs/10.1002/qj.3654>.
- Fernando Garcia, Juan Ruiz, Paola Salio, Hernan Bechis, and Steve Nesbitt. Argentina mesonet data. Version 1.1. UCAR/NCAR - earth observing laboratory. URL <https://doi.org/10.26023/JEXB-W6B6-E310>.
- Nicholas A. Gasperoni, Xuguang Wang, Keith A. Brewster, and Frederick H. Carr. Assessing Impacts of the High-Frequency Assimilation of Surface Observations for the Forecast of Convection Initiation on 3 April 2014 within the Dallas–Fort Worth Test Bed. *146(11):3845–3872*. ISSN 1520-0493, 0027-0644. doi: 10.1175/MWR-D-18-0177.1. URL <https://journals.ametsoc.org/view/journals/mwre/146/11/mwr-d-18-0177.1.xml>.
- Luis G. Goncalves de Goncalves, Luiz Sapucci, Eder Vendrasco, João Gerd de Mattos, Camila Ferreira, Eduardo Khamis, and Nicolas Cruz. A rapid update data assimilation cycle over South America using 3DVar and EnKF. In *The 20th International TOVS Study Conference (ITSC-20)*. The 20th International TOVS Study Conference (ITSC-20).
- G. A. Grell and S. R. Freitas. A scale and aerosol aware stochastic convective parameterization for weather and air quality modeling. *13(9):23845–23893*. ISSN 1680-7375. doi: 10.5194/acpd-13-23845-2013. URL <https://www.atmos-chem-phys-discuss.net/13/23845/2013/>.
- So-Young Ha and Chris Snyder. Influence of Surface Observations in Mesoscale Data Assimilation Using an Ensemble Kalman Filter. *142(4):1489–1508*. ISSN 0027-0644, 1520-0493. doi: 10.1175/MWR-D-13-00108.1. URL <http://journals.ametsoc.org/doi/10.1175/MWR-D-13-00108.1>.
- Y Han, Paul Van Delst, Q Liu, F. Weng, B. Yan, Russ Treadon, and John Derber. JCSDA Community Radiative Transfer Model (CRTM)—version 1. URL https://repository.library.noaa.gov/view/noaa/1157/noaa_1157_DS1.pdf.
- Song-You Hong, Ju-Hye Kim, Jeong-ock Lim, and Jimy Dudhia. The WRF Single Moment 6-Class Microphysics Scheme (WSM6). *42: 129–151*, a.
- Song-You Hong, Yign Noh, and Jimy Dudhia. A New Vertical Diffusion Package with an Explicit Treatment of Entrainment Processes. *134(9):2318–2341*, b. ISSN 0027-0644, 1520-0493. doi: 10.1175/MWR3199.1. URL <http://journals.ametsoc.org/doi/10.1175/MWR3199.1>.
- Ming Hu, Guoqing Ge, Chunhua Zhou, Don Stark, Hui Shao, Kathryn Newman, Jeff Beck, and Xin Zhang. Grid-point Statistical Interpolation (GSI) User's Guide Version 3.7. URL <https://dtcenter.org/community-code/gridpoint-statistical-interpolation-gsi/documentation>.
- George Huffman, David Bolvin, Dan Braithwaite, Kuolin Hsu, Robert Joyce, Christopher Kidd, Eric Nelkin, S. Sorooshian, J. Tan, and Pingping Xie. NASA Global Precipitation Measurement (GPM) Integrated Multi-satellite Retrievals for GPM (IMERG). URL https://docserver.gesdisc.eosdis.nasa.gov/public/project/GPM/IMERG_ATBD_V5.pdf.
- Brian R. Hunt, Eric J. Kostelich, and Istvan Szunyogh. Efficient data assimilation for spatiotemporal chaos: A local ensemble transform Kalman filter. *230(1-2):112–126*. ISSN 01672789. doi: 10.1016/j.physd.2006.11.008. URL <https://linkinghub.elsevier.com/retrieve/pii/S0167278906004647>.
- Michael J. Iacono, Jennifer S. Delamere, Eli J. Mlawer, Mark W. Shephard, Shepard A. Clough, and William D. Collins. Radiative forcing by long-lived greenhouse gases: Calculations with the AER radiative transfer models. *113(D13):D13103*. ISSN 0148-0227. doi: 10.1029/2008JD009944. URL <http://doi.wiley.com/10.1029/2008JD009944>.
- Zaviša I. Janjić. The Step-Mountain Eta Coordinate Model: Further Developments of the Convection, Viscous Sublayer, and Turbulence Closure Schemes. *122(5):927–945*. ISSN 0027-

- 1117 0644. doi: 10.1175/1520-0493(1994)122<0927:TSMECM>2.0.CO;2¹⁸⁸
 1118 2. URL <https://journals.ametsoc.org/doi/10.1175/1520-0493%1189>
 1119 281994%29122%3C0927%3ATSMECM%3E2.0.CO%3B2.¹⁹⁰
- 1120 Thomas A. Jones, Jason A. Otkin, David J. Stensrud, and Kent Knopfmeier. Assimilation of Satellite Infrared Radiances and Doppler Radar Observations during a Cool Season Observing System Simulation Experiment. 141(10):3273–3299. ISSN 0027-0644, 1520-0493. doi: 10.1175/MWR-D-12-00267.1. URL [https://journals.ametsoc.org/doi/10.1175/MWR-D-12-00267.1.](https://journals.ametsoc.org/doi/10.1175/MWR-D-12-00267.1)¹⁹⁶
- 1121 John S Kain. The Kain–Fritsch Convective Parameterization: An Update. 43:12.¹⁹⁸
- 1122 UCAR/NCAR Earth Observing Laboratory. Multi-network composite highest resolution radiosonde data. Version 1.3. UCAR/NCAR earth observing laboratory. URL <https://doi.org/10.26023/GKFF>²⁰⁰
- 1123 YNBJ-BV14.²⁰²
- 1124 Haidao Lin, Stephen S. Weygandt, Stanley G. Benjamin and Ming Hu. Satellite Radiance Data Assimilation within the Hourly Updated Rapid Refresh. 32(4):1273²⁰⁴
 1125 1287. ISSN 0882-8156. doi: 10.1175/WAF-D-16-0215.²⁰⁶
 1126 URL <https://journals.ametsoc.org/waf/article/32/4/1273/41099>²⁰⁷
- 1127 Satellite-Radiance-Data-Assimilation-within-the.²⁰⁸
- 1128 Yasumitsu Maejima, Takemasa Miyoshi, Masaru Kunii, Hiromu Seko and Kae Sato. Impact of Dense and Frequent Surface Observations on 1-Minute-Update Severe Rainstorm Prediction: A Simulation Study. 97(1):253–273. doi: 10.2151/jmsj.2019-014.²¹²
- 1129 Paula Maldonado, Juan Ruiz, and Celeste Saulo. Sensitivity to Initial and Boundary Perturbations in Convective-Scale Ensemble-Based Data Assimilation: Imperfect-Model OSSEs. 17(0):96–102. ISSN 1349-6476. doi: 10.2151/sola.2021-015. URL https://www.jstage.jst.go.jp/article/sola/17/0/17_2021-015/_article.²¹⁶
- 1130 Swapan Mallik and Thomas A. Jones. Assimilation of GOES-16 satellite derived winds into the warn-on-forecast system 245:105131. ISSN 0169-8095. doi: 10.1016/j.atmosres.2020.105131. URL <https://www.sciencedirect.com/science/article/pii/S016980952031067X>.²²⁰
- 1131 Paul Markowski and Yvette Richardson. Organization of Isolated Convection. In *Mesoscale Meteorology in Midlatitudes*, pages 201–244. John Wiley & Sons, Ltd. ISBN 978-0-470-68210-4. doi: 10.1002/9780470682104.ch8. URL <https://onlinelibrary.wiley.com/doi/abs/10.1002/9780470682104.ch8>.²²⁴
- 1132 C. Matsudo, Yanina García Skabar, Juan Ruiz, Luciano Vidal, and Paola Salio. Verification of WRF-ARW convective-resolving forecasts over Southeastern South America. 66:445–456.²²⁸
- 1133 Mikio Nakanishi and Hiroshi Niino. Development of an Improved Turbulence Closure Model for the Atmospheric Boundary Layer. 87(5):895–912. ISSN 0026-1165. doi: 10.2151/jmsj.87.895. URL <https://doi.org/10.2151/jmsj.87.895?from=CrossRef>.²³²
- 1134 National Centers for Environmental Prediction, National Weather Service, NOAA, U.S. Department of Commerce. NCEP GFS 0.25 degree global forecast grids historical archive. URL <https://doi.org/10.5065/D65D8PWK>.²³⁷
- 1135 Tobias Necker, Stefan Geiss, Martin Weissmann, Juan Ruiz, Takemasa Miyoshi, and Guo-Yuan Lien. A convective-scale 1,000-member ensemble simulation and potential applications. 146(728):1423²⁴¹
 1136 1442. ISSN 0035-9009, 1477-870X. doi: 10.1002/qj.3744. URL <https://onlinelibrary.wiley.com/doi/abs/10.1002/qj.3744>.²⁴²
- 1137 Stephen W. Nesbitt, Paola V. Salio, Eldo Ávila, Phillip Bitzen, Lawrence Carey, V. Chandrasekar, Wiebke Deierling, Francina Dominguez, Maria Eugenia Dillon, C. Marcelo Garcia, David Gochis, Steven Goodman, Deanna A. Hence, Karen A. Kosiba, Matthew R. Kumjian, Timothy Lang, Lorena Medina Luna, James Marquis, Robert Marshall, Lynn A. McMurdie, Ernani Lima Nascimento, Kristen L. Rasmussen, Rita Roberts, Angela K. Rowe, Juan José Ruiz, Eliah F. M. T. São Sabbas, A. Celeste Saulo, Russ Schumacher, Yanina Garcia Skabar, Luiz Augusto Toledo Machado, Robert J. Trapp, Adam Varble, James Wilson, Joshua Wurman, Edward J. Zipser, Ivan Arias, Hernán Bechis, and Maxwell A. Groves. A storm safari in Subtropical South America: Proyecto RELAM-PAGO. -1:1–64. ISSN 0003-0007, 1520-0477. doi: 10.1175/BAMS-D-20-0029.1. URL <https://journals.ametsoc.org/view/journals/bams/aop/BAMS-D-20-0029.1/BAMS-D-20-0029.1.xml>.²⁵⁴
- 1138 Michiko Otsuka, Masaru Kunii, Hiromu Seko, Kazuki Shimoji, Masahiro Hayashi, and Koji Yamashita. Assimilation Experiments of MTSAT Rapid Scan Atmospheric Motion Vectors on a Heavy Rainfall Event. 93(4):459–475. doi: 10.2151/jmsj.2015-030.
- 1139 Rachida El Ouaraihi, Loïk Berre, Claude Fischer, and El Hassan Sayouty. Sensitivity of regional ensemble data assimilation spread to perturbations of lateral boundary conditions. 67(1):28502. ISSN null. doi: 10.3402/tellusa.v67.28502. URL <https://doi.org/10.3402/tellusa.v67.28502>.
- 1140 Kristen L. Rasmussen, Manuel D. Zuluaga, and Robert A. Houze. Severe convection and lightning in subtropical South America. 41(20):7359–7366. ISSN 1944-8007. doi: 10.1002/2014GL061767. URL <https://agupubs.onlinelibrary.wiley.com/doi/abs/10.1002/2014GL061767>.
- 1141 Brett Roberts, Burkely T. Gallo, Israel L. Jirak, Adam J. Clark, David C. Dowell, Xuguang Wang, and Yongming Wang. What Does a Convection-Allowing Ensemble of Opportunity Buy Us in Forecasting Thunderstorms? 35(6):2293–2316. ISSN 0882-8156, 1520-0434. doi: 10.1175/WAF-D-20-0069.1. URL <https://journals.ametsoc.org/view/journals/wefo/35/6/WAF-D-20-0069.1.xml>.
- 1142 Nigel Roberts. Assessing the spatial and temporal variation in the skill of precipitation forecasts from an NWP model. 15(1):163–169. ISSN 1469-8080. doi: 10.1002/met.57. URL <https://rmets.onlinelibrary.wiley.com/doi/abs/10.1002/met.57>.
- 1143 Juan J. Ruiz, Celeste Saulo, and Julia Nogués-Paegle. WRF Model Sensitivity to Choice of Parameterization over South America: Validation against Surface Variables. 138(8):3342–3355. ISSN 0027-0644. doi: 10.1175/2010MWR3358.1. URL <https://journals.ametsoc.org/mwr/article/138/8/3342/71137/WRF-Model-Sensitivity-to-Choice-of>.
- 1144 Masahiro Sawada, Zaizhong Ma, Avichal Mehra, Vijay Tallapragada, Ryo Oyama, and Kazuki Shimoji. Impacts of Assimilating High-Resolution Atmospheric Motion Vectors Derived from Himawari-8 on Tropical Cyclone Forecast in HWRF. 147(10):3721–3740. ISSN 1520-0493, 0027-0644. doi: 10.1175/MWR-D-18-0261.1. URL <https://journals.ametsoc.org/view/journals/mwre/147/10/mwr-d-18-0261.1.xml>.
- 1145 Hui Shao, John Derber, Xiang-Yu Huang, Ming Hu, Kathryn Newman, Donald Stark, Michael Lueken, Chunhua Zhou, Louisa Nance, Ying-Hwa Kuo, and Barbara Brown. Bridging Research to Operations Transitions: Status and Plans of Community GSI. 97(8):1427–1440. ISSN 0003-0007, 1520-0477. doi: 10.1175/BAMS-D-13-0045.1. URL <https://journals.ametsoc.org/doi/10.1175/BAMS-D-13-0045.1>.
- 1146 Randhir Singh, Satya P. Ojha, C. M. Kishtawal, P. K. Pal, and A. S. Kiran Kumar. Impact of the assimilation of INSAT-3D radiances on short-range weather forecasts: Assimilation of INSAT-3D Radiances. 142(694):120–131. ISSN 00359009. doi: 10.1002/qj.2636. URL <http://doi.wiley.com/10.1002/qj.2636>.
- 1147 William C Skamarock, Joseph B Klemp, Jimy Dudhia, David O Gill, Dale M Barker, Michael G Duda, Xiang-Yu Huang, Wei Wang, and Jordan G Powers. A Description of the Advanced Research WRF Version 3.
- 1148 Ryan A. Sobash and David J. Stensrud. Assimilating Surface Mesonet Observations with the EnKF to Improve Ensemble Forecasts of Convection Initiation on 29 May 2012. 143(9):3700–3725. ISSN 1520-0493, 0027-0644. doi: 10.1175/MWR-D-14-00126.1. URL <https://journals.ametsoc.org/view/journals/mwre/143/9/mwr-d-14-00126.1.xml>.
- 1149 Juanzhen Sun, Ming Xue, James W. Wilson, Isztar Zawadzki, Sue P. Ballard, Jeanette Onylee-Hooimeyer, Paul Joe, Dale M. Barker, Ping-Wah Li, Brian Golding, Mei Xu, and James Pinto. Use of NWP for Nowcasting Convective Precipitation: Recent Progress and Challenges. 95(3):409–426. ISSN 0003-0007, 1520-0477. doi: 10.1175/BAMS-D-11-00263.1. URL <https://journals.ametsoc.org/view/journals/bams/95/3/bams-d-11-00263.1.xml>.
- 1150 Zheng Qi Wang and Roger Randriamampianina. The Impact of Assimilating Satellite Radiance Observations in the Copernicus European Regional Reanalysis (CERRA). 13(3):426. ISSN 2072-4292. doi: 10.3390/rs1303426. URL <https://www.mdpi.com/2072-4292/13/3/426>.

- 1259 Peter Weston, Alan Geer, Niels Bormann, and Niels Bormann. Investigations into the assimilation of AMSU-A in the presence of
 1260 cloud and precipitation. ISSN 50.
- 1261
- 1262 DUSTAN M. WHEATLEY and DAVID J. STENSrud. The Impact of
 1263 Assimilating Surface Pressure Observations on Severe Weather
 1264 Events in a WRF Mesoscale Ensemble System. 138(5):1673–
 1265 1694. ISSN 1520-0493, 0027-0644. doi: 10.1175/2009MWR3042.
 1266 1. URL <https://journals.ametsoc.org/view/journals/mwre/138/5/2009mwr3042.1.xml>.
- 1267
- 1268 Jeffrey S. Whitaker and Thomas M. Hamill. Evaluating Methods to
 1269 Account for System Errors in Ensemble Data Assimilation. 140
 1270 (9):3078–3089. ISSN 0027-0644, 1520-0493. doi: 10.1175/MWR-D-
 1271 11-00276.1. URL <http://journals.ametsoc.org/doi/10.1175/MWR-D-11-00276.1>.
- 1272
- 1273 Ting-Chi Wu, Hui Liu, Sharanya J. Majumdar, Christopher S. Velden,
 1274 and Jeffrey L. Anderson. Influence of Assimilating Satellite-Derived
 1275 Atmospheric Motion Vector Observations on Numerical Analyses
 1276 and Forecasts of Tropical Cyclone Track and Intensity. 142(1):
 1277 49–71. ISSN 1520-0493, 0027-0644. doi: 10.1175/MWR-D-13-
 1278 00023.1. URL <https://journals.ametsoc.org/view/journals/mwre/142/1/mwr-d-13-00023.1.xml>.
- 1279
- 1280 Juan Zhao, Jidong Gao, Thomas A. Jones, and Junjun Hu. Impact of Assimilating High-Resolution Atmospheric Motion Vectors on Convective Scale Short-Term Forecasts: 1. Observing System Simulation Experiment (OSSE). 13(10):e2021MS002484,
 1281 a. ISSN 1942-2466. doi: 10.1029/2021MS002484. URL <https://onlinelibrary.wiley.com/doi/abs/10.1029/2021MS002484>.
- 1282
- 1283 Juan Zhao, Jidong Gao, Thomas A. Jones, and Junjun Hu. Impact of Assimilating High-Resolution Atmospheric Motion Vectors on Convective Scale Short-Term Forecasts: 2. Assimilation Experiments of GOES-16 Satellite Derived Winds. 13(10):e2021MS002486,
 1284 b. ISSN 1942-2466. doi: 10.1029/2021MS002486. URL <https://onlinelibrary.wiley.com/doi/abs/10.1029/2021MS002486>.
- 1285
- 1286 Kefeng Zhu, Ming Xue, Yujie Pan, Ming Hu, Stanley G. Benjamin,
 1287 Stephen S. Weygandt, and Haidao Lin. The Impact of Satellite
 1288 Radiance Data Assimilation within a Frequently Updated Regional
 1289 Forecast System Using a GSI-based Ensemble Kalman Filter. 36
 1290 (12):1308–1326, a. ISSN 0256-1530, 1861-9533. doi: 10.1007/
 1291 s00376-019-9011-3. URL <http://link.springer.com/10.1007/s00376-019-9011-3>.
- 1292
- 1293 Yanqiu Zhu, John Derber, Andrew Collard, Dick Dee, Russ Treadon,
 1294 George Gayno, and James A. Jung. Enhanced radiance bias
 1295 correction in the National Centers for Environmental Prediction's
 1296 Gridpoint Statistical Interpolation data assimilation system. 140
 1297 (682):1479–1492, b. ISSN 1477-870X. doi: 10.1002/cj.2233. URL
 1298 <https://rmets.onlinelibrary.wiley.com/doi/abs/10.1002/cj.2233>.
- 1299
- 1300 Yanqiu Zhu, Emily Liu, Rahul Mahajan, Catherine Thomas, David
 1301 Groff, Paul Van Delst, Andrew Collard, Daryl Kleist, Russ Treadon,
 1302 and John C. Derber. All-Sky Microwave Radiance Assimilation in
 1303 NCEP's GSI Analysis System. 144(12):4709–4735, c. ISSN 0027-
 1304 0644. doi: 10.1175/MWR-D-15-0445.1. URL <https://journals.ametsoc.org/doi/full/10.1175/MWR-D-15-0445.1>.
- 1305
- 1306
- 1307
- 1308
- 1309
- 1310